

THE LOW-REDSHIFT INTERGALACTIC MEDIUM AS SEEN IN ARCHIVAL LEGACY HUBBLE/STIS AND FUSE DATA

EVAN M. TILTON, CHARLES W. DANFORTH AND J. MICHAEL SHULL

CASA, Department of Astrophysical and Planetary Sciences, University of Colorado, 389-UCB, Boulder, CO 80309;
evan.tilton@colorado.edu, charles.danforth@colorado.edu, michael.shull@colorado.edu

AND

TERESA L. ROSS

Department of Astronomy, New Mexico State University, Las Cruces, NM 88003; rosst@nmsu.edu

Submitted to The Astrophysical Journal.

ABSTRACT

We present a comprehensive catalog of ultraviolet (*HST*/STIS and *FUSE*) absorbers in the low-redshift IGM at $z < 0.4$. The catalog draws from the extensive literature on IGM absorption, and it reconciles discrepancies among previous catalogs through a critical evaluation of all reported absorption features in light of new *HST*/COS data. We report on 746 H I absorbers down to a rest-frame equivalent width of 12 mÅ over a maximum redshift path length $\Delta z = 5.38$. We also confirm 111 O VI absorbers, 29 C IV absorbers, and numerous absorption features due to other metal ions. We characterize the distribution of absorber line frequency as a function of column density as a power law, $dN/dz \propto N^{-\beta}$, where $\beta = 2.08 \pm 0.12$ for O VI and $\beta = 1.68 \pm 0.03$ for H I. Utilizing a more sophisticated accounting technique than past work, the catalog accounts for $\sim 43\%$ of the baryons: $24 \pm 2\%$ in the photoionized Ly α forest and $19 \pm 2\%$ in the WHIM as traced by O VI. We discuss the large systematic effects of various assumed metallicities and ionization states on these calculations, and we implement recent simulation results in our estimates.

Subject headings: cosmological parameters — cosmology: observations — intergalactic medium — quasars: absorption lines — ultraviolet: general

1. INTRODUCTION

The successful connection of recent advances in cosmology to the processes that shape the low-redshift universe requires a detailed understanding of the intergalactic medium (IGM). Simulations (e.g., Cen & Ostriker 1999; Davé et al. 2001; Smith et al. 2011) predict that a large portion of the baryonic mass of the universe resides in the non-luminous IGM in the form of primordial gas and gas processed by galaxies. The systematic characterization of these systems in absorption at different redshifts is thus a key step toward understanding the evolution of galaxies and the universe in general.

At high-redshift, the diffuse photoionized IGM, commonly known as the Ly α forest, accounts for nearly all of the baryonic matter, but simulations and observations both find that this fraction is reduced to $\sim 30\%$ by $z \sim 0$ (e.g., Davé et al. 2001; Penton et al. 2000). Many of the remaining baryons reside in the “warm-hot” IGM (WHIM) phase, which is heated to 10^{5-7} K as gas is shocked during gravitational infall, cloud-cloud collisions, and by galaxy winds (Cen & Fang 2006). Because of their low density, these phases of the IGM are most readily observed in absorption against a background continuum source such as an AGN, using Lyman series H I lines as well as highly ionized metal species such as C IV and O VI. As these features lie in the rest-frame far-ultraviolet (FUV), recent low redshift ($z \lesssim 0.4$) studies (e.g., Danforth et al. 2006; Danforth & Shull 2005, 2008; Lehner et al. 2007; Thom & Chen 2008; Tripp et al. 2008) have focused on observations with the *Far Ultraviolet Spectroscopic Explorer* (*FUSE*) and the Space Telescope Imaging Spec-

trograph (STIS) on the *Hubble Space Telescope* (*HST*). Together, these studies suggest that the column density distribution of H I follows a power law, $dN/dN \propto N^{-\beta}$, where $\beta \sim 1.7$, and that highly ionized metals such as O VI follow a similar distribution with $\beta \sim 2$.

With the installation of the Cosmic Origins Spectrograph (COS) on *HST*, our sensitivity in the FUV is at an all-time high, and we have the opportunity to probe the IGM more deeply than ever before. With more than ten times the sensitivity of STIS, COS (Green et al. 2012) promises to probe the IGM with a larger and more systematic selection of sight lines down to lower column densities. Already, a large number of targets have been observed (e.g., Danforth et al. 2010, 2011; Narayanan et al. 2011; Savage et al. 2011a). A systematic understanding of existing STIS and *FUSE* data in light of the early COS data, however, is essential to guiding future IGM studies. To this end, we present in this work a systematic catalog of STIS and *FUSE* IGM absorbers, the largest such catalog to date, in light of past studies and new COS data. We draw primarily from the extensive literature in this field, creating a comprehensive database of IGM absorbers that reconciles discrepancies among previous lists of absorbers. It contains 746 H I and 111 O VI absorbers, as well as detections of many other ion species, along 44 AGN sight-lines. We further present new counting statistics and cosmological parameters derived from the catalog, and we compare these results to other work in the field. This catalog will lay the groundwork for future COS IGM studies.

2. METHODOLOGY

2.1. *Sight-Line Selection and Data Reduction*

The primary goal of this catalog is to create the most comprehensive low-redshift IGM census possible with legacy STIS and *FUSE* data. Therefore, we included all 44 sight lines with $z_{AGN} \lesssim 0.5$ for which STIS/E140M and/or *FUSE* data were available at reasonable quality. The imposed high-redshift cutoff guarantees STIS wavelength coverage of nearly all potential Ly α features while avoiding complications in interpretation due to high densities of IGM absorption features present in higher-redshift sight lines ($z \sim 1-2$). All data have a resolution of 20 km s^{-1} or better at a signal-to-noise ratio per resolution element $(S/N)_{\text{res}} \gtrsim 5$ in most cases. The *FUSE* data provide wavelength coverage over $905 - 1187 \text{ \AA}$, while, in most cases, STIS/E140M covers $1162 - 1729 \text{ \AA}$. A few of the sight-lines (3C 273, Akn 564, Mrk 509, Mrk 205, and PG 1116+215) lack the longest wavelength order of the STIS/E140M data and truncate at 1709 \AA . The data were supplemented by COS data in a few cases to assist in the confirmation and interpretation of absorption features as described in Section 2.2. These COS data add additional coverage over $1135 - 1770 \text{ \AA}$ at a resolution of $\sim 15 \text{ km s}^{-1}$ and a S/N that greatly improves upon the *FUSE* and STIS data in most cases. We used all COS data available for these sight lines as of 2011 September 28. Table 1 summarizes the final sample of sight lines and data, which cover a total Ly α redshift pathlength of $\Delta z = 5.38$.

The STIS data were reduced as described in our group’s previous paper on this subject (Danforth & Shull 2008, hereafter DS08), and the *FUSE* data were reduced as described by Danforth et al. (2006). We relied primarily on the highest throughput *FUSE* channel, LiF1 (Moos et al. 2000), but we also used the LiF2 and SiC channels to aid in interpretation and to provide coverage where the LiF1 data were absent, suspect, or of low S/N. The COS data were reduced as described in Danforth et al. (2010).

2.2. *Catalog Construction*

The creation of the catalog was designed as a critical analysis of previously published lists of absorption features in the low-redshift IGM. We began by correlating the features reported in a variety of sources, summarized in Table 2, for all sight lines in our sample. Although some of the sight lines were analyzed in only one previous work, many have been studied by two or more groups. One sight line, Ton S210, has data from *FUSE*, STIS, and COS, but it has not been included in any major, multi-ion IGM absorption survey. As such, our analysis of that sight line is original. Each feature was individually inspected in the data, and its interpretation, in terms of both structure and identification, was confirmed in context with related lines. We used any available COS data to aid in the interpretation of each feature, but the measurements themselves were not made from the COS data. Although the COS data sometimes refute the existence of features that are seen by the other instruments, the features were nevertheless included in the catalog so as to maintain a homogeneous sample; they were, however, flagged as suspect. For cases in which our interpretation

and all existing literature measurements agreed in the basic interpretation of the feature, we computed consensus values for the observed wavelength, rest-frame equivalent width and Doppler b -values as means of the measurements reported in the literature. One-sigma errors were computed assuming that the measurements were independent. This assumption, while not formally accurate, is roughly approximated by differences in data reduction, continuum placement, and measurement technique. As a complementary measure of the error, we also computed the mean absolute deviation among the individual measurements. In cases where one or more of the sources disagreed on the interpretation of the feature, we critically evaluated the arguments and data and either chose the best interpretation or, if necessary, remeasured the feature before proceeding as in the case of total agreement. If appropriate, alternate identifications and structural interpretations were noted. Throughout this process, a number of previously unreported features were found serendipitously. Although we measured them and included them in the catalog, we note that this project was not a systematic search for new absorption systems, owing to its literature-based nature. Every redshift with an H I absorption system, however, was checked for corresponding absorption in each of the metal ions listed in Table 3.

When we measured a feature’s properties, we used either the apparent optical depth (AOD) method (Sembach & Savage 1992) or a Voigt profile fit (see discussion in Danforth et al. 2006, and sources therein). We qualitatively judged which method was most appropriate for each feature, taking into account the two methods’ relative strengths. Although the two methods usually generate comparable results, the AOD method performs better for weak lines or in extremely noisy regions of the spectra, while profile fitting is preferable for strong or blended lines or lines with complicated component structure (DS08). Where necessary, we adopted the atomic parameters given by Morton (2003) or, for lines not included in that work, from the NIST Atomic Spectra Database (Ralchenko et al. 2010).

We took a conservative approach to the splitting of absorption features into separate components. In cases where clear separation was visible or multiple lines of the same absorber showed consistent asymmetry, we favored multiple-component interpretations. On the other hand, if separation into components was ambiguous, we favored a single-component interpretation, even if the overall profile shape suggested the presence of multiple components. Where possible, we used high-S/N COS data to further inform our interpretation of the component structure. This approach leaves the catalog with few, if any, false positives in terms of measured components, but some features may have more components than reported here. For comparison, the features reported in this catalog yield counting statistics intermediate between those of DS08, which generally used single-component interpretations, and the profile-fitting results of Tripp et al. (2008), who generally used many-component interpretations. Our component splitting is comparable to that of Thom & Chen (2008). Differences in component-splitting approaches are expected to have little impact on the calculation of baryon densities because the primary methods used to derive those quanti-

TABLE 1
44 AGN SIGHTLINES AND DATA USED IN THE CATALOG

Sight Line	R.A. (J2000.0)	Decl. (J2000.0)	z_{AGN}	STIS (ksec)	FUSE (ksec)	COS/G130M (ksec)	COS/G160M (ksec)
Mrk 335	00 06 19.5	+20 12 10	0.0258	17.1	97.0	2.4	1.6
IZw1	00 53 34.9	+12 41 36.0	0.0607	...	38.6
Ton S180	00 57 20.0	-22 22 59.3	0.0620	...	16.6
Ton S210	01 21 51.5	-28 20 57	0.1160	22.5	53.3	5.0	5.5
Fairall 9	01 23 46.0	-58 48 23.8	0.0461	...	38.9
HE 0226-4410	02 28 15.2	-40 57 16	0.4950	43.8	33.2	6.7	7.8
NGC 985	02 34 37.8	-08 47 15.6	0.0431	...	68.0
PKS 0312-770	03 11 55.2	-76 51 51	0.2230	8.4	5.5
PKS 0405-123	04 07 48.4	-12 11 37	0.5726	27.2	71.1	22.2	11.1
Akn 120	05 16 11.4	-00 08 59.4	0.0331	...	56.2
HS 0624+6907	06 30 02.5	+69 05 04	0.3700	62.0	112.3
VII Zw118	07 07 13.1	+64 35 58.8	0.0797	...	198.6
PG 0804+761	08 10 58.5	+76 02 41.9	0.1000	...	174.0	6.7	6.3
Ton 951	08 47 42.5	+34 45 03.5	0.0640	...	31.9
PG 0953+414	09 56 52.4	+41 15 22	0.2341	8.0	72.1
Ton 28	10 04 02.5	+28 55 35	0.3297	33.0	11.2
3C 249.1	11 04 13.7	+76 58 58	0.3115	68.8	216.8
Mrk 421	11 04 27.3	+38 12 32.0	0.0300	...	83.9	1.7	2.4
PG 1116+215	11 19 08.6	+21 19 18	0.1765	26.5	77.0
PG 1211+143	12 14 17.7	+14 03 13	0.0809	42.5	52.3
PG 1216+069	12 19 20.9	+06 38 38	0.3313	5.8	12.0
Mrk 205	12 21 44.0	+75 18 38	0.0708	62.1	203.6
3C 273	12 29 06.7	+02 03 09	0.1583	18.7	42.3
Q 1230+0115	12 30 50.0	+01 15 23	0.1170	9.8	4.0	11.1	8.1
PG 1259+593	13 01 12.9	+59 02 07	0.4778	95.8	668.3	9.2	11.2
PKS 1302-102	13 05 33.0	-10 33 19	0.2784	4.8	142.7	7.0	6.9
Mrk 279	13 53 03.4	+69 18 30	0.0305	54.6	228.5	2.2	2.7
NGC 5548	14 17 59.5	+25 08 12	0.0172	69.8	55.0	1.9	2.4
Mrk 1383	14 29 06.6	+01 17 06	0.0865	10.5	63.5
Mrk 817	14 36 22.1	+58 47 39.5	0.0313	...	189.9	3.4	3.0
Mrk 478	14 42 07.5	+35 26 22.9	0.0791	...	14.2
PG 1444+407	14 46 45.9	+40 35 06	0.2673	48.6	10.0
Mrk 290	15 35 52.4	+57 54 09.3	0.0296	...	12.8	3.9	4.8
Mrk 876	16 13 57.2	+65 43 10	0.1290	29.2	46.0	12.6	11.8
3C 351	17 04 41.4	+60 44 31	0.3719	77.0	141.9
H 1821+643	18 21 57.3	+64 20 36	0.2970	50.9	132.3	0.6	0.5
PKS 2005-489	20 09 25.4	-48 49 53.9	0.0710	...	49.2	2.5	1.9
Mrk 509	20 44 09.7	-10 43 25	0.0344	7.6	62.3	9.0	16.5
II Zw136	21 32 27.8	+10 08 19.4	0.0630	...	22.7
PHL 1811	21 55 01.5	-09 22 25	0.1900	33.9	75.0	3.5	3.1
PKS 2155-304	21 58 52.0	-30 13 32	0.1160	10.8	123.2
Akn 564	22 42 39.3	+29 43 31	0.0247	10.3	60.9	1.7	2.4
MR 2251-178	22 54 05.8	-17 34 55.0	0.0644	...	54.1
NGC 7469	23 03 15.6	+08 52 26	0.0163	22.8	44.3	1.9	1.8

TABLE 2
SOURCES OF DATA USED IN THE CATALOG

Number ^a	Reference	Number ^a	Reference
1	Williger et al. (2006)	12	Sembach et al. (2004)
2	Danforth & Shull (2008)	13	Richter et al. (2004)
3	Thom & Chen (2008)	14	Jenkins et al. (2003)
4	Prochaska et al. (2004)	15	Narayanan et al. (2011)
5	Lehner et al. (2007)	16	Tripp et al. (2008, Table 3)
6	Tripp et al. (2008, Table 2)	17	Savage et al. (2005)
7	Sembach et al. (2001)	18	Danforth et al. (2006)
8	Tripp et al. (2001)	19	Howk et al. (2009)
9	Oegerle et al. (2000)	20	Richter et al. (2001)
10	Aracil et al. (2006)	21	Tumlinson et al. (2005)
11	Savage et al. (2002)	22	Lehner et al. (2006)

^a Identifying number used in the catalog.

TABLE 3
PRIMARY IGM DIAGNOSTIC LINES

Ion	λ_{rest} (Å)	f^a	$[X/H]_{\odot}^b$	f_{ion}^c CIE	$\log T_{\text{max}}$
H I	1215.67	0.4164	0.00		$< 4.19^d$
	1025.72	0.07914	0.00		$< 4.19^d$
Fe II	1144.94	0.0830	-4.50	0.79	$4.05 - 4.27^d$
	1063.18	0.0547	-4.50	0.79	$4.05 - 4.27^d$
C II	1334.53	0.128	-3.57	0.97	$4.15 - 4.66^d$
	1036.34	0.118	-3.57	0.97	$4.15 - 4.66^d$
Si II	1260.42	1.18	-4.49	0.97	$< 4.30^d$
	1193.29	0.582	-4.49	0.97	$< 4.30^d$
S II	1259.52	0.0166	-4.88	1.00	$< 4.47^d$
	1253.81	0.0109	-4.88	1.00	$< 4.47^d$
Fe III	1122.52	0.0544	-4.50	0.89	$4.27 - 4.58^d$
Si III	1206.50	1.63	-4.49	0.90	$4.30 - 4.85^d$
C III	977.02	0.757	-3.57	0.83	$4.66 - 5.01^d$
S III	1012.50	0.0438	-4.88	0.84	$4.47 - 4.93^d$
	1190.20	0.0237	-4.88	0.84	$4.47 - 4.93^d$
Si IV	1393.76	0.513	-4.49	0.35	4.8^e
	1402.70	0.254	-4.49	0.35	4.8^e
C IV	1548.20	0.190	-3.57	0.29	5.0^e
	1550.77	0.0948	-3.57	0.29	5.0^e
S IV	1062.66	0.0494	-4.88	0.61	$4.93 - 5.13^d$
N V	1238.82	0.156	-4.17	0.24	5.25^e
	1242.80	0.0777	-4.17	0.24	5.25^e
O VI	1031.93	0.1325	-3.31	0.22	5.45^e
	1037.62	0.0658	-3.31	0.22	5.45^e

^a Absorption line oscillator strength (Morton 2003).

^b Solar photospheric element abundance, $\log(X/H)$ (Asplund et al. 2009).

^c Peak ion fraction under CIE (Sutherland & Dopita 1993).

^d Temperature range ion is dominant under CIE (Sutherland & Dopita 1993).

^e Ion is never dominant under CIE; temperature is peak CIE abundance.

ties depend only on the total column density observed.

After compiling complete lists of the properties of individual absorption lines from a given system, we took a similar approach in determining the consensus properties of the absorber inferred from those lines. In cases where only a single line was present for the absorber, the Doppler b -value was taken to be the same as the mean value for the feature. The column density was computed as the geometric mean of the literature values, with errors treated as above. In many cases, more than one absorption line was present for the absorber. For metal species with multiple lines, we proceeded as with single-line detections but used a mean weighted by the expected relative strengths of the observed absorption lines. If any of the lines was deemed suspect, for example because of excessive noise or blending, it was not included in the mean. The H I absorbers were treated in a more complicated fashion, because, in addition to allowing measurements of the individual Lyman series lines, the ion is particularly conducive to curve-of-growth (COG) analyses (see discussion in Danforth et al. 2006) when multiple lines are present. In cases of agreement among the various literature sources, we were able to compute simple mean values for the column density and b -value of the absorber as above. However, if any remeasurement or reinterpretation was necessary at the level of individual absorption lines, we used either new COG analyses or new weighted means of the line measurements to determine the Doppler b -values and column densities for the absorber. In these consensus mean at the absorber level, we also included measurements from literature sources that did not report properties for the individual absorption

lines. In a few cases with extremely high column density H I, we estimated the absorber parameters by fitting the integrated absorptin from higher Lyman lines (i.e., the Lyman decrement), if sufficiently short-wavelength data were available. The vast majority of H I absorbers, however, show only Ly α absorption, and in those cases the absorber-level properties were inferred directly from that single line.

Because the various literature sources differ slightly in their approach to reporting their measurements, we made minor adjustments to our general approach in individual cases. Tripp et al. (2008) report both total equivalent width and column density for each absorption complex as well as profile-fitting measurements of individual components; we used the relevant measurements as appropriate to our interpretation of the structure of the feature. In using the measurements of the Lehner et al. (2006) study of the HE 0226-4110 sight line, we adopted the AOD equivalent width and Doppler b -value measurements and the profile-fitting column density measurements. The Williger et al. (2006) study of the PKS 0405-123 sight line employed a methodological approach that resulted in a large number of very weak H I detections which, from an examination of the COS data, seem to be noise features rather than real absorption features. While we have included these measurements in the catalog for the sake of completeness, their equivalent widths and column densities have been flagged as upper limits to avoid biasing the sample set. Similarly, the Richter et al. (2004) study of the PG 1259+593 sight line reports a large number of “probable” Ly α detections. All were re-evaluated in light of the much higher S/N COS data and included in our catalog, but, as with the Williger et al. (2006) paper, we flagged those that seem to be noise as upper limits rather than measurements. Finally, Richter et al. (2004) report a variety of measurements for each detected feature. For metal features, we favored the profile-fitting measurements where available and otherwise used the AOD measurements. For H I, we used the profile-fitting measurements for individual features and, when possible, the COG measurements for ion-level absorber properties.

A number of features in the catalog are reported as upper limits, owing to excessive blending, weakness relative to noise, or for the reasons described in the previous paragraph. In these cases, we reported the most conservative limit from the references, which may be either a measured value in the case of blended lines or a limit based on the noise characteristics of the data. Because upper limits are treated somewhat differently among different authors, we report a minimum S/N-based equivalent width for each feature for the sake of consistency:

$$W_{\text{min}} = \frac{4\lambda}{7200(S/N)_{\lambda}}(1+z)^{-1}. \quad (1)$$

This quantity roughly corresponds to a 4σ significance level in equivalent width for the data in the rest frame of the absorber. It assumes a resolved feature with $b = 25 \text{ km s}^{-1}$, roughly the median b -value for H I and O VI, with the factor of 7200 corresponding to the resolution, $R = \lambda/\Delta\lambda$, required to resolve a line with that b -value. The signal-to-noise, (S/N), was calculated as the ratio of mean flux to its standard deviation in the smoothed continuum. Features with equivalent widths near or be-

low the reported value of W_{\min} should be viewed with skepticism and treated as upper limits. Note, however, that these 4σ estimates do not account for fixed-pattern noise, which is mitigated by the smoothing applied during the data reduction, or for other systematic effects.

Table 4 presents the complete catalog of individual absorption lines. Columns (1) through (4) identify the feature according to sight line, observed wavelength, redshift, and transition, respectively. Column (5) lists an “ion code” that correlates absorption lines within a sight line in Table 4 with the associated absorber properties in Table 5. Columns (6) through (9) describe the measured strength of the feature. Column (6) is a flag that identifies the rest-frame equivalent width listed in Column (7) as a normal measurement (“n”), an upper limit (“<”), a lower limit (“>”), or an order-of-magnitude estimate (“~”) when a reliable measurement could not be obtained. Column (8) is the mean absolute deviation of the measurements used to generate that consensus value. Column (9) identifies the sources or techniques used to construct the consensus value, with every two-digit portion of the value in the table corresponding to a source listed in Table 2. Other numbers are used to identify our own measurements: 23 corresponds to a Voigt fit, 24 corresponds to an AOD measurement, 25 corresponds to a COG measurement, and 26 corresponds to a Lyman decrement estimate. Columns (10) through (13) report on the velocity width of the feature in terms of the Doppler b -parameter in the same format in which the equivalent width measurements were reported. Column (14) lists the quantity W_{\min} as defined in Equation 1 and evaluated at the observed wavelength. Column (15) lists possible alternate line identifications in the rare case that identification was ambiguous. Finally, Column (16) flags inconsistencies between the COS data (where available) and the STIS and/or FUSE data. No flag is present if COS data are absent or in agreement with the other data, while flags are listed for features that are entirely absent from the COS data (“a”), weaker or partially absent in the COS data (“p”), or that display a different shape or structure in the COS data (“d”).

Table 5 presents the complete catalog of absorbers. Columns (1) through (3) identify the absorber via the sight line, redshift, and ion species, respectively. Column (4) reports the ion code that correlates Tables 4 and 5, as described in the the previous paragraph. Using a similar format to the measurements in Table 4, Columns (5) through (7) report on the column density of the absorber, with Column (5) identifying the type of measurement with the same set of flags used in Table 5, Column (6) reporting the column density, and Column (7) reporting the references or techniques used to generate the measurement, again as in Table 4. Columns (8) through (10) report on the measurements of the Doppler b -parameter in the same manner.

2.3. Absorber Statistics

In compiling absorber statistics, we followed the approach of DS08. We focus on fourteen ions, listed in Table 3 along with some of their properties. For all statistics and derived quantities, we included only absorbers in the redshift range $500 \text{ km s}^{-1} < cz < (cz_{\text{AGN}} - 1500 \text{ km s}^{-1})$ and further required that $z < 0.4$. These limits help to exclude absorbers intrinsic to either the Milky Way or the

background AGN while also ensuring that the sample is restricted to the local, low-redshift universe where sensitive H I measurements via the Ly α transition can be obtained. We further excluded all absorbers at $z > 0.104$ in the Q1230+115 sight line ($z_{\text{AGN}} = 0.1170$) because these features are likely intrinsic to the AGN (Ganguly et al. 2003). Despite these velocity limits, some high-velocity AGN outflow systems may contribute to our sample. These limits are less restrictive than those adopted by Tripp et al. (2008) and comparable to those adopted by DS08.

For each ion species, we constructed simple histograms of the number of absorbers in 0.2 dex bins in $\log N$, as well as distributed histograms in which each detection is characterized by a Gaussian (DS08). We proceeded to calculate the number of absorbers per unit redshift,

$$\frac{dN(\log N)}{dz} = \sum_i \frac{N_i(\log N_i)}{\Delta z_i}. \quad (2)$$

This quantity is a function of column density, N , because it must be corrected for incompleteness. The correction is achieved by dividing the number, N_i , per bin by an effective redshift path length, Δz_i , which is itself a function of column density and accounts for variations in sensitivity to the absorption feature in question.

We establish this redshift pathlength by considering the S/N in the continuum of the highest-S/N data covering a given wavelength. This $(S/N)_\lambda$ vector was rebinned to a resolution comparable to the data. The smoothed, normalized flux was then used to mask $(S/N)_\lambda$ such that areas of saturated absorption were set to $(S/N)_\lambda = 0$ while regions of unsaturated absorption were scaled with the optical depth, τ_λ , as $(S/N)_\lambda \propto (\tau_\lambda + 1)^{-1}$. This approach effectively removes lines of any type from the effective pathlength. The resulting vector was converted to a 4σ minimum equivalent width vector defined, as in DS08, by

$$W_{\min} = \frac{4\lambda}{R(S/N)_\lambda} \quad (3)$$

where the instrumental resolution, $R = \lambda/\Delta\lambda$, was set to 15,000 or 42,000 for *FUSE* or STIS data, respectively. The effective redshift pathlength for singlet lines is then simply the total path length over all sightlines such that $W_\lambda > W_{\min}$. This is easily extended to multiplet lines of different line strengths ($f\lambda$) by requiring, in the rest frame of the weaker line, that either $W_\lambda > W_{\min}(z_1)$ or $W_\lambda > [W_{\min}(z_2)](f_1\lambda_1/f_2\lambda_2)$.

Uncertainty in dN/dz is dominated by the uncertainty in absorber number (N_i) per bin due to Poisson statistics (Gehrels 1986). Inherent uncertainty in effective redshift pathlength Δz_i is negligible, but this quantity contributes uncertainty arising from its variation over the width of a column density bin. We approximate this uncertainty as

$$d(\Delta z_i) = \frac{1}{8} [(\Delta z)_{i+1} - (\Delta z)_{i-1}], \quad (4)$$

as suggested by DS08, in which these two sources of error were added in quadrature.

TABLE 4
 IGM ABSORPTION LINE PROPERTIES

Sight Line (1)	λ_{obs} (Å) (2)	z (3)	Line (4)	Ion # (5)	W Flag (6)	W (mÅ) (7)	W_{MAD} (mÅ) (8)	Ref. (9)	b Flag (10)	b (km/s) (11)	b_{MAD} (km/s) (12)	Ref. (13)	W_{min} (14)	Alt. ID (15)	COS (16)
3C249	1596.95	0.31364	Ly α	1	n	148 \pm 8		06	n	13 \pm 1		23	21.0		
3C249	1591.56	0.30920	Ly α	2	n	30 \pm 3		02	n	8 \pm 1		02	29.0		
3C249	1590.21	0.30809	Ly α	3	n	262 \pm 17		02	n	33 \pm 1		02	29.0		
3C249	1589.95	0.30788	Ly α	4	n	68 \pm 19		02	n	22 \pm 4		02	29.0		
3C249	1573.39	0.29426	Ly α	5	n	40 \pm 8		02	n	10 \pm 1		02	28.9		
3C249	1544.16	0.27021	Ly α	6	n	73 \pm 16		02	~	43		02	47.9		
3C249	1539.82	0.26664	Ly α	7	n	96 \pm 8		02	n	67 \pm 19		02	51.2		
3C249	1537.49	0.26473	Ly α	8	n	210 \pm 19		02	n	33 \pm 2		02	44.5		
3C249	1532.51	0.27021	Si III1207	9	n	18 \pm 6		02	~	19		02	44.2		
3C249	1515.64	0.24676	Ly α	10	n	452 \pm 16	17	0206	n	39 \pm 1		02	51.1		
3C249	1512.24	0.24396	Ly α	11	n	473 \pm 23		02	n	56 \pm 2		02	55.4		
3C249	1511.47	0.24332	Ly α	12	n	317 \pm 27		02	n	53 \pm 3		02	55.4		
3C249	1510.34	0.24239	Ly α	13	n	176 \pm 20		02	n	41 \pm 3		02	55.4		
3C249	1505.34	0.23828	Ly α	14	n	164 \pm 25		02	n	14 \pm 1		02	56.1		
3C249	1504.27	0.24681	Si III1207	15	n	22 \pm 9		23	n	7 \pm 3		23	55.7		
3C249	1459.93	0.20093	Ly α	16	n	78 \pm 18		02	n	12 \pm 2		02	57.2		
3C249	1459.63	0.20068	Ly α	17	n	312 \pm 11		02	n	34 \pm 3		02	57.2		
3C249	1458.69	0.17371	N V1243	18	<	17		02					58.4		
3C249	1455.10	0.19695	Ly α	19	n	57 \pm 4		02	~	43		02	42.5		
3C249	1454.02	0.17371	N V1239	18	n	29 \pm 4		02	n	24 \pm 7		02	43.3		
3C249	1441.77	0.18599	Ly α	20	n	53 \pm 10		02	n	23 \pm 4		02	35.9		
3C249	1429.54	0.17593	Ly α	21	n	238 \pm 36		02	n	39 \pm 6		02	49.8		
3C249	1429.06	0.17553	Ly α	22	n	244 \pm 39		02	n	41 \pm 6		02	49.8		
3C249	1426.84	0.17371	Ly α	23	n	49 \pm 12		02	n	29 \pm 5		02	27.0		
3C249	1423.54	0.17099	Ly α	24	n	34 \pm 10		23	n	23 \pm 5		23	27.0		
3C249	1412.80	0.17099	Si III1207	25	n	16 \pm 3		02	~	10		02	31.5		
3C249	1410.87	0.16057	Ly α	26	n	73 \pm 10		02	n	29 \pm 3		02	31.2		
3C249	1396.38	0.24396	Fe III1123	27	n	16 \pm 3		02	~	4		02	24.8		
3C249	1391.01	0.11925	N V1243	28	<	10		02					32.0		
3C249	1388.09	0.14183	Ly α	29	n	278 \pm 10		02	n	38 \pm 1		02	31.3		
3C249	1386.55	0.11925	N V1239	28	n	11 \pm 2		02	~	15		02	32.5		
3C249	1384.73	0.13907	Ly α	30	n	27 \pm 9		02	n	25 \pm 7		02	31.9		
3C249	1379.42	0.13470	Ly α	31	n	64 \pm 3		02	n	65 \pm 2		02	25.1		
3C249	1368.50	0.12572	Ly α	32	n	373 \pm 21		02	n	31 \pm 1		02	28.7		
3C249	1368.07	0.12536	Ly α	33	n	151 \pm 21		02	n	43 \pm 5		02	28.7		
3C249	1363.05	0.31364	O VII1038	34	n	22 \pm 11		06	n	14 \pm 2		23	24.7		

NOTE. — Table 4 is published in its entirety in the electronic edition of the Astrophysical Journal. A portion is shown here for guidance regarding its form and content. A complete description of the columns in this table can be found in Section 2.2 of the text.

2.4. Baryon Fraction

Studies of the cosmic microwave background (Komatsu et al. 2011) have provided accurate measurements of the cosmological baryon density, $\Omega_b = 0.0455 \pm 0.0028$, as a fraction of the critical density of the universe, $\rho_{\text{cr}} = (3H_0^2/8\pi G) = (9.205 \times 10^{-30} \text{ g cm}^{-3})h_{70}^2$ for a Hubble constant, $H_0 = (70 \text{ km s}^{-1} \text{ Mpc}^{-1})h_{70}$. The majority of this matter, both at high and low redshift, must reside in the IGM. A complete accounting of IGM baryons at low redshift is therefore best studied with a combination of FUV and X-ray spectroscopy (Shull et al. 2011). We address the former here with our catalog, which traces IGM gas at $T \lesssim 10^6 \text{ K}$, by considering H I absorbers in the Ly α forest and metal species as tracers of the WHIM.

2.4.1. Metal Ions

We present two quantities that measure baryon density contributions as traced by metal ions. In both cases, we use five equally spaced bins in z , and we assume a mean atomic mass, $\mu = 1.32m_{\text{H}}$, for $Y_{\text{He}} = 0.2477$ (Peimbert et al. 2007). The contribution to the critical

density by the IGM mass of an ion is given by

$$\begin{aligned}
 \Omega_{\text{ion}} &= \frac{H_0 m_{\text{ion}}}{c \rho_{\text{cr}}} \\
 &\times \int_0^{z_{\text{max}}} \int_{N_{\text{min}}}^{N_{\text{max}}} \frac{dN(\log N)}{dz} N d(\log N) dz \\
 &= (1.365 \times 10^{-23} \text{ cm}^2) h_{70}^{-1} (m_{\text{ion}}/\text{amu}) \\
 &\times \sum_{j=0}^{z_{\text{max}}} \sum_{i=\log N_{\text{min}}}^{\log N_{\text{max}}} \left(\left[\frac{dN(\log N)}{dz} \right]_{i,j} \langle N \rangle_{i,j} \right. \\
 &\quad \left. \times \Delta \log N \frac{\Delta z_j}{z_{\text{max}}} \right), \quad (5)
 \end{aligned}$$

where m_{ion} is the ion mass and the integration is over column density (cm^{-2}) and redshift path length. We report the uncertainty in Ω_{ion} as the asymmetric Poisson uncertainty in dN evaluated at the mean dz , $\langle z \rangle$, and $\langle N \rangle$ weighted by dN .

While Ω_{ion} is the observed contribution to the critical density by a given ion, we are also interested in estimating the total baryonic density of all species as traced by a particular ion. We denote this estimate as $\Omega_{\text{IGM}}^{(\text{ion})}$; it

TABLE 5
IGM ABSORBER PROPERTIES

Sight Line	z	Ion	Ion code	N Flag	$\log N$ (N in cm^{-2})	Ref.	b Flag	b (km s^{-1})	Ref.
(1)	(2)	(3)	(4)	(5)	(6)	(7)	(8)	(9)	(10)
3C249	0.31364	HI	1	n	13.976 ± 0.021	1623	n	12.5 ± 0.6	1623
3C249	0.30920	HI	2	n	12.720 ± 0.040	02	n	8.0 ± 1.0	02
3C249	0.30809	HI	3	n	13.860 ± 0.085	02	n	35.7 ± 5.6	02
3C249	0.30788	HI	4	n	13.050 ± 0.140	02	n	22.0 ± 4.0	02
3C249	0.29426	HI	5	n	12.860 ± 0.080	02	n	10.0 ± 1.0	02
3C249	0.27021	HI	6	n	13.210 ± 0.125	02	~	43	02
3C249	0.26664	HI	7	n	13.320 ± 0.075	02	n	67.0 ± 19.0	02
3C249	0.26473	HI	8	n	13.900 ± 0.100	02	n	27.5 ± 4.5	02
3C249	0.27021	Si III	9	n	12.030 ± 0.190	02	~	19	02
3C249	0.24676	HI	10	n	14.460 ± 0.067	0203	n	37.2 ± 1.2	0203
3C249	0.24396	HI	11	n	14.200 ± 0.035	02	n	56.9 ± 4.7	02
3C249	0.24332	HI	12	n	13.940 ± 0.080	02	n	52.8 ± 8.7	02
3C249	0.24239	HI	13	n	13.800 ± 0.055	02	n	30.7 ± 3.8	02
3C249	0.23828	HI	14	n	13.840 ± 0.120	02	n	14.0 ± 1.0	02
3C249	0.24681	Si III	15	n	12.099 ± 0.125	0323	n	8.4 ± 3.2	0323
3C249	0.20093	HI	16	n	13.250 ± 0.100	02	n	12.0 ± 2.0	02
3C249	0.20068	HI	17	n	13.970 ± 0.090	02	n	38.5 ± 8.9	02
3C249	0.17371	NV	18	n	13.190 ± 0.130	02	n	24.0 ± 7.0	02
3C249	0.19695	HI	19	n	13.080 ± 0.090	02	~	43	02
3C249	0.18599	HI	20	n	12.970 ± 0.070	02	n	23.0 ± 4.0	02
3C249	0.17593	HI	21	n	13.740 ± 0.060	02	n	39.0 ± 6.0	02

NOTE. — Table 5 is published in its entirety in the electronic edition of the Astrophysical Journal. A portion is shown here for guidance regarding its form and content. A complete description of the columns in this table can be found in Section 2.2 of the text.

TABLE 6
SUMMARY OF IGM DETECTIONS AND RESULTS

Ion	$\mathcal{N}_{\text{total}}$	\mathcal{N}	z_{abs}	Δz_{max}	$d\mathcal{N}/dz^{\text{a}}$ ($> 10 \text{ m}\text{\AA}$)	$d\mathcal{N}/dz^{\text{a}}$ ($> 21 \text{ m}\text{\AA}$)	$d\mathcal{N}/dz^{\text{a}}$ ($> 30 \text{ m}\text{\AA}$)	β
(1)	(2)	(3)	(4)	(5)	(6)	(7)	(8)	(9)
O VI	118	111	< 0.40	6.095	$42.0^{+10.7}_{-6.3}$	$27.7^{+3.8}_{-2.9}$	$22.2^{+3.2}_{-2.4}$	2.075 ± 0.119
N V	29	25	< 0.396	5.408	$70.4^{+47.1}_{-24.1}$	$20.6^{+8.2}_{-5.1}$	$9.6^{+5.4}_{-2.7}$	2.001 ± 0.235
C IV	36	29	< 0.116	2.523	$14.3^{+4.5}_{-2.5}$	$14.3^{+4.5}_{-2.5}$	$11.7^{+3.7}_{-2.0}$	1.774 ± 0.157
C III	51	50	< 0.40	5.644	$23.8^{+10.3}_{-4.7}$	$17.3^{+4.7}_{-2.7}$	$14.4^{+3.7}_{-2.2}$	1.859 ± 0.092
Si IV	34	30	< 0.24	4.317	$15.4^{+6.7}_{-3.0}$	$11.8^{+4.0}_{-2.1}$	$9.2^{+3.5}_{-1.8}$	1.729 ± 0.125
Si III	62	57	< 0.40	5.244	$16.6^{+4.1}_{-2.6}$	$10.4^{+2.4}_{-1.5}$	$7.4^{+2.1}_{-1.2}$	1.739 ± 0.102
HI	797	746	< 0.40	5.382	$283.9^{+57.2}_{-32.8}$	$175.2^{+13.0}_{-9.8}$	$144.0^{+6.6}_{-6.0}$	1.680 ± 0.030
Poorly Constrained Ion Species								
Fe III	15	11	< 0.40	5.853	$9.3^{+5.2}_{-2.6}$	$5.4^{+4.2}_{-1.8}$	$3.7^{+3.5}_{-1.4}$	2.216 ± 0.428
C II	18	18	< 0.296	4.900	$9.6^{+5.3}_{-2.2}$	$8.0^{+3.7}_{-1.8}$	$7.5^{+3.5}_{-1.7}$	1.587 ± 0.121
Fe II	5	4	< 0.40	5.913	$11.2^{+13.8}_{-5.0}$	$4.3^{+7.0}_{-2.5}$	$4.3^{+7.0}_{-2.5}$	1.922 ± 1.505
Si II	15	15	< 0.372	5.345	$7.1^{+3.6}_{-1.7}$	$7.1^{+3.6}_{-1.7}$	$6.1^{+3.3}_{-1.5}$	1.568 ± 0.157
S II	3	3	< 0.373	5.352	$10.0^{+13.4}_{-4.8}$	$6.2^{+10.1}_{-3.6}$	$3.1^{+7.1}_{-2.5}$	1.568 ± 0.157
S III ^b	1	1	< 0.40	5.924
S IV ^b	0	0	< 0.40	5.889
N II ^c	8	8
N III ^c	3	3

^a Number of absorbers per unit redshift path length, integrated down to the indicated equivalent width.

^b No statistics are presented for this ion species owing to a lack of detections.

^c Though several detections of this ion are reported in the catalog, no systematic search was made for this species. As a result, all detections were serendipitous and any statistics derived from those detections may be heavily biased. We therefore refrain from reporting any such statistics but note the detections for completeness.

is obtained by correcting Ω_{ion} for metallicity and ionization fraction. Generally, we assume a metallicity of $Z = 0.1Z_{\odot}$ (DS08) and an ionization fraction equal to the peak collisional ionization equilibrium (CIE) ion abundance, f_{ion} , listed in Table 3, but we discuss alternate choices for the product Zf_{ion} in Section 3.3. The quantity $\Omega_{\text{IGM}}^{(\text{ion})}$ is thus

$$\begin{aligned} \Omega_{\text{IGM}}^{(\text{ion})} &= \left(\frac{H_0}{c\rho_{\text{cr}}}\right)^2 \frac{\mu m_H}{Z(M/H)_{\odot} f_{\text{ion}}} \\ &\times \int_0^{z_{\text{max}}} \int_{N_{\text{min}}}^{N_{\text{max}}} \frac{d\mathcal{N}(\log N_{\text{ion}})}{dz} \langle N_{\text{ion}} \rangle d(\log N_{\text{ion}}) dz \\ &= \frac{1.83 \times 10^{-23} h_{70}^{-1} \text{cm}^2}{Z(M/H)_{\odot} f_{\text{ion}}} \\ &\times \sum_{j=0}^{z_{\text{max}}} \sum_{i=\log N_{\text{min}}}^{\log N_{\text{max}}} \left(\left[\frac{d\mathcal{N}(\log N_{\text{ion}})}{dz} \right]_{i,j} \langle N_{\text{ion}} \rangle_{i,j} \right. \\ &\quad \left. \times \Delta \log N_{\text{ion}} \frac{\Delta z_j}{z_{\text{max}}} \right), \end{aligned} \quad (6)$$

where the factor of $\Delta z_j/z_{\text{max}}$ weights the contribution of each bin in dz . Uncertainties in $\Omega_{\text{IGM}}^{(\text{ion})}$ are calculated as for Ω_{ion} ; systematic uncertainties arising from our assumptions are not included. Additional systematic uncertainties in this quantity likely exist due to effects of nonequilibrium ionization, photoionization, or deviations from the assumed 10% solar metallicity. Shull et al. (2011) looked into these effects in detail, especially with respect to O VI, and we discuss them further in Section 3.3

2.4.2. The Ly α Forest

The Ly α forest is an important reservoir of baryons, with previous surveys finding up to $\sim 30\%$ the total baryonic content of the universe in this photoionized phase of the IGM at low redshift (e.g., Penton et al. 2000; Lehner et al. 2007; Danforth & Shull 2008). As the catalog presented here contains the largest sample of Ly α forest absorbers to date, with a total Ly α redshift path-length $\Delta z = 5.38$, it provides useful constraints on $\Omega_{\text{IGM}}^{(\text{HI})}$, the fraction of baryons found in the forest. To this end, we use three methods of calculating that quantity: the methods of Penton et al. (2000, 2004), Schaye (2001), and Shull et al. (2011).

The method of Penton et al. (2000) assumes that Ly α forest absorbers are singular isothermal spheres and further assumes an impact parameter, p , scaled here as $p = (100 \text{ kpc})p_{100}$. As a result, the assumptions of this method are only valid for H I absorbers at fairly low column density ($\log N \lesssim 14.5$). The method adopts an approximate, frequency-integrated H I photoionization rate given by,

$$\Gamma_{\text{HI}} \approx (2.49 \times 10^{-14} \text{ s}^{-1}) J_{-23} \left(\frac{4.8}{\alpha_s + 3} \right), \quad (7)$$

where $J_{-23} = 1$ is the ionizing radiation field at 1 Rydberg in units of $10^{-23} \text{ ergs cm}^{-2} \text{ s}^{-1} \text{ Hz sr}^{-1}$ and α_s is the spectral index of the radiation field, set to $\alpha_s = 1.8$. Thus, scaling the H I column density as

$N_{\text{HI}} = (10^{14} \text{ cm}^{-2})N_{14}$, we can define

$$\begin{aligned} \Omega_{\text{IGM}}^{(\text{HI})} &= \frac{(1.59 \times 10^9 M_{\odot})H_0 (p_{100}^5 J_{-23} [4.8/(\alpha_s + 3)])^{1/2}}{c\pi p^2 \rho_{\text{cr}}} \\ &\times \int_0^{z_{\text{max}}} \int_{N_{\text{min}}}^{N_{\text{max}}} \frac{d\mathcal{N}(N_{\text{HI}})}{dz} N_{14}^{1/2} d(N_{\text{HI}}) dz \\ &= 8.73 \times 10^{-5} h_{70}^{-1} \left(J_{-23} p_{100} \frac{4.8}{\alpha_s + 3} \right)^{1/2} \\ &\times \sum_{j=0}^{z_{\text{max}}} \sum_{i=\log N_{\text{min}}}^{\log N_{\text{max}}} \left[\frac{d\mathcal{N}(\log N_{\text{HI}})}{dz} \right]_{i,j} N_{14}^{1/2} \frac{\Delta z_j}{z_{\text{max}}}. \end{aligned} \quad (8)$$

Our preferred method for low column density absorbers, however, is the revised method of Shull et al. (2011). Although this method retains the assumptions of Penton et al. (2000) regarding the scale and geometry of the IGM clouds, it also includes redshift-dependent corrections for the evolution in the space density of absorbers, $\phi(z) \propto (1+z)^3$, as well as the hydrogen photoionization rate. Haardt & Madau (2012) found a rapid increase in the metagalactic ionizing background radiation from $z = 0$ to $z = 0.7$, fitted by Shull et al. (2011) to the form,

$$\Gamma_{\text{HI}} = (2.28 \times 10^{-14} \text{ s}^{-1})(1+z)^{4.4}. \quad (9)$$

Thus, scaling the electron temperature as $T = (10^{4.3} \text{ K})T_{4.3}$, they obtain,

$$\begin{aligned} \Omega_{\text{IGM}}^{(\text{HI})} &= (9.0 \times 10^{-5}) \frac{h_{70}^{-1} p_{100}^{1/2} T_{4.3}^{0.363} (1+z)^{0.2}}{[\Omega_m (1+z)^3 + \Omega_{\Lambda}]^{1/2}} \\ &\times \int_0^{z_{\text{max}}} \int_{N_{\text{min}}}^{N_{\text{max}}} \frac{d\mathcal{N}(\log N_{\text{HI}})}{dz} N_{14}^{1/2} d(\log N_{\text{HI}}) dz \\ &= (9.0 \times 10^{-5}) h_{70}^{-1} p_{100}^{1/2} T_{4.3}^{0.363} \\ &\times \sum_{j=0}^{z_{\text{max}}} \sum_{i=\log N_{\text{min}}}^{\log N_{\text{max}}} \left(\frac{(1+z_j)^{0.2}}{[\Omega_m (1+z_j)^3 + \Omega_{\Lambda}]^{1/2}} \right. \\ &\quad \left. \times \left[\frac{d\mathcal{N}(\log N_{\text{HI}})}{dz} \right]_{i,j} N_{14}^{1/2} \frac{\Delta z_j}{z_{\text{max}}} \right). \end{aligned} \quad (10)$$

Finally, we apply the method described by Schaye (2001). This formalism assumes that the IGM clouds are gravitationally bound and that the observed column densities are characteristic over the local Jeans length. We expect that these assumptions better characterize high column density absorbers ($\log N_{\text{HI}} \gtrsim 14.5$) than do the other methods. Hence, scaling the temperature as $T = (10^4 \text{ K})T_4$, they define,

$$\begin{aligned} \Omega_{\text{IGM}}^{(\text{HI})} &= (1.46 \times 10^{-4}) h_{70}^{-1} \Gamma_{-12}^{1/3} T_4^{0.59} \\ &\times \int_0^{z_{\text{max}}} \int_{N_{\text{min}}}^{N_{\text{max}}} \frac{d\mathcal{N}(N_{\text{HI}})}{dz} N_{14}^{1/3} d(N_{\text{HI}}) dz \\ &= (1.46 \times 10^{-4}) h_{70}^{-1} \Gamma_{-12}^{1/3} T_4^{0.59} \\ &\times \sum_{j=0}^{z_{\text{max}}} \sum_{i=\log N_{\text{min}}}^{\log N_{\text{max}}} \left(\left[\frac{d\mathcal{N}(\log N_{\text{HI}})}{dz} \right]_{i,j} \right. \\ &\quad \left. \times N_{14}^{1/3} \frac{\Delta z_j}{z_{\text{max}}} \right), \end{aligned} \quad (11)$$

where we set $\Gamma_{\text{HI}} = 0.03 \times 10^{-12} \text{ s}^{-1}$ at $z \sim 0$ (Shull et al. 1999; Weymann et al. 2001).

For all methods, we assume a temperature of $T = 2 \times 10^4 \text{ K}$ and sum over bins in column density and redshift. We set $p_{100} = 1$ and normalize to $N_{14} = 1$ throughout. For our Δz pathlength in $\text{Ly}\alpha$, cosmic variance is expected to contribute insignificantly to the errors, which instead are dominated by Poisson error (Penton et al. 2004). We therefore calculate the error in $\Omega_{\text{IGM}}^{(\text{HI})}$ as the one-sided Poisson error (Gehrels 1986) in $dN(d \log N, dz)$ bins summed in quadrature.

2.4.3. Note on Inconsistencies in DS08

The calculations of contributions to Ω by both metals and H I were described and calculated inconsistently in DS08 owing to incorrect cosmological factors. The baryon fractions listed in their Tables 12 and 13 were computed with incorrect cosmological corrections that differed from those given in Equations 7–10 of DS08 and consequently overestimated values of Ω_b for all ions discussed. Our new *HST* archive survey properly includes these effects, as well as the redshift evolution of the hydrogen photoionization rate, $\Gamma_H(z)$. The original baryon fraction values tabulated in DS08 are unsuitable for comparison to other observations or simulations, though the absorber statistics that do not depend on dX (e.g., dN/dz) remain valid. Detailed corrections of the data tables will be submitted as an erratum. For the sake of comparison to the present work, we briefly describe the issue here.

DS08 calculated contributions to Ω_b using a redshift-invariant path length dX instead of dz , but the definition of dX was applied inconsistently. The text described the conventional “absorption pathlength function” of Bahcall & Peebles (1969):

$$dX \equiv (1+z)^2 [\Omega_m(1+z)^3 + \Omega_\Lambda]^{-1/2} dz, \quad (12)$$

but the calculations incorrectly implemented the pathlength function as

$$dX \equiv (1+z)^{-1} [\Omega_m(1+z)^3 + \Omega_\Lambda]^{-1/2} dz. \quad (13)$$

The difference in the two formalisms is a factor of $(1+z)^3$, negligible at $z \sim 0$ but a factor of ~ 3 at the highest redshifts surveyed. As a result, the corrected dN/dX values using the proper formalism as presented in the erratum are lower than those published in Table 11 of DS08 by 25–39% for most ion species. Because C IV is only seen at $z \lesssim 0.1$ in the STIS/E140M data, its value of dN/dX only decreases by roughly 13%.

The cosmological parameters Ω_{ion} and $\Omega_{\text{IGM}}^{(\text{ion})}$ (DS08, Equations 6 and 8 and Table 12) scale with dN/dX . Recalculating the values of Table 12 with the correct dX treatment results in a $\sim 40\%$ decrease in the values of $\Omega_{\text{IGM}}^{(\text{ion})}$ in most cases ($\sim 12\%$ for C IV). Interestingly, this $\sim 40\%$ decrease in $\Omega_{\text{IGM}}^{(\text{OVI})}/\Omega_b$ brings the DS08 value more in line with other published values at the same sensitivity limits.

The overall baryon density accounted for by $\text{Ly}\alpha$ absorbers (Equations 9 and 10 of DS08) suffer similar adjustments, changing to $\Omega_{\text{IGM}}^{(\text{HI})}/\Omega_b = 20.7 \pm 2.4\%$ if calculated with the Penton et al. (2004) method and

$\Omega_{\text{IGM}}^{(\text{HI})}/\Omega_b = 17.5 \pm 2.6\%$ if calculated with the Schaye (2001) method over a column density range, $12.5 < \log N_{\text{HI}} < 16.5$. These adjusted values still do not account for the redshift evolution of $\Gamma_H(z) \propto (1+z)^{4.4}$ which is included in the method of Shull et al. (2011) as applied to the present paper’s catalog and enters the equation as the square root.

All further references in the present paper to values of Ω_b reported by DS08 refer to the corrected values.

3. RESULTS AND DISCUSSION

3.1. Properties of the Catalog

3.1.1. Comparison to Previous O VI Catalogs

As previously discussed, a number of studies have been undertaken to study the WHIM as traced by FUV O VI absorption, most notably DS08, Tripp et al. (2008), and Thom & Chen (2008). Each of these studies broadly used the same STIS data sets, albeit with independent reduction processes, some minor variation in sight-line selection, and with various degrees of assistance from *FUSE* data. Their line selection and measurement methodologies, however, vary considerably, and produce significantly different catalogs. Figure 1 presents column-density histograms of the O VI detections reported by each of those catalogs, as well as the catalog presented here. As these variations can lead to different inferences and derived quantities, they must be kept in mind when interpreting this work or comparing studies of the WHIM. Though this discussion focuses on O VI, it is analogous to the distributions of other ion species.

The differences in the catalogs can be attributed primarily to the line selection criteria as well as approach to splitting detected features into subcomponents. In terms of detection criteria, DS08 took an inclusive approach indexed to $\text{Ly}\alpha$, in which any feature detected at 4σ or greater at close to the appropriate wavelength was included. DS08’s approach to component splitting, however, was conservative: most blended lines were reported as a single absorption feature and most clearly split metal lines were reported together if the associated H I absorption was of ambiguous structure. Together, these approaches lead to more detections at low column densities (some of which may be erroneous identifications), fewer detections at intermediate column densities, and a flatter histogram when compared to other catalogs. In addition, a few O VI absorbers with little or no H I absorption at the same redshift were missed in that study. In contrast, Thom & Chen (2008) took a very conservative approach to inclusion, requiring that both lines of the O VI doublet be detected blindly without reference to H I. This leads to fewer detections overall, especially at low column densities. Subcomponents are split more liberally than in DS08. Finally, Tripp et al. (2008) took an approach that combined the two aforementioned methods. The O VI doublets were identified blindly before a second search pass looked for O VI at redshifts suggested by strong absorption from other ions. The issue of subcomponents was avoided by presenting two sets of measurements: one that considered absorption “systems” with no splitting and one that split the systems into all discernable components. As a result, the histogram for their “component” detections is strongly peaked at intermediate column densities, while their systemic measurements

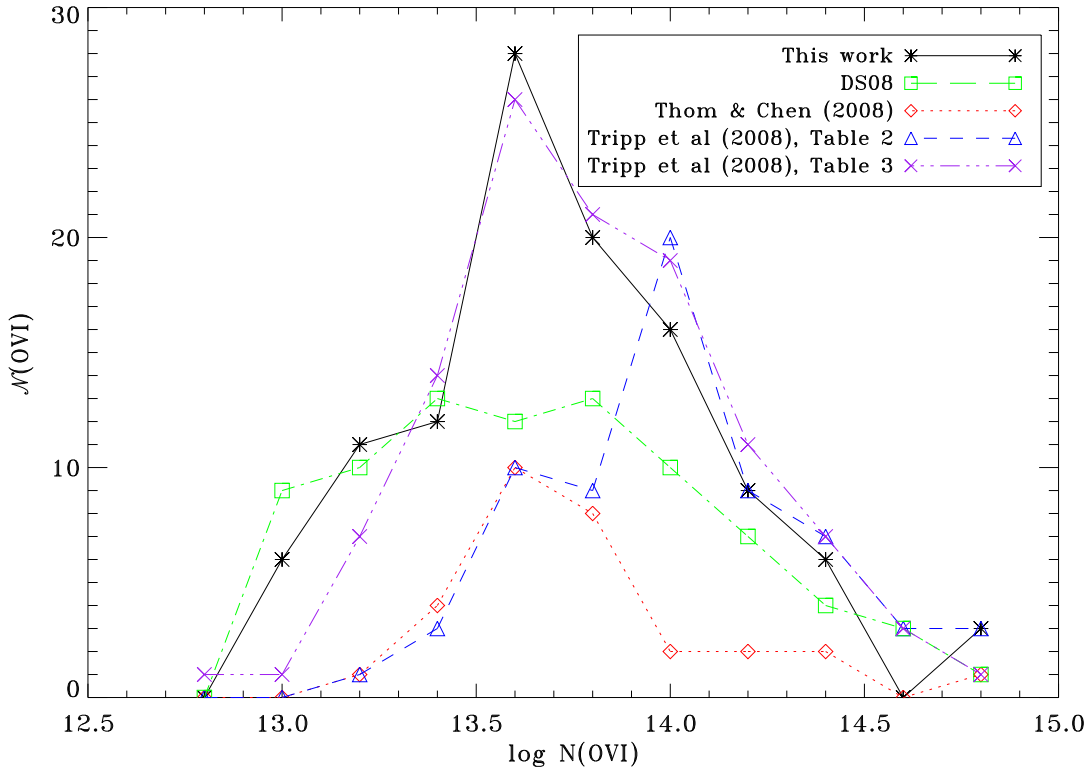


FIG. 1.— Histograms comparing O VI detections as reported in this work, DS08, Tripp et al. (2008), and Thom & Chen (2008). Bins in $\log N_{\text{OVI}}$ are 0.2 dex in width, centered on the plotted points. The two separate sets of points for Tripp et al. (2008) represent their “system” (Table 2) and “component” (Table 3) measurements. Our catalog and component results of Tripp et al. (2008) are strongly peaked at $\log N_{\text{OVI}} \approx 13.6$.

lead to a distribution shifted to high column densities and reduced in total number of detections.

As described in Section 2.2, our catalog is intermediate in its approach to component splitting compared to the aforementioned studies. It includes all reasonable detections included in previous catalogs that are not contradicted by new COS data. As a result, it is the largest catalog in terms of number of H I and O VI detections. The O VI distribution is strongly peaked at $\log N \approx 13.2$, and it contains an intermediate number of detections at lower column densities compared to DS08 and Tripp et al. (2008). Compared to DS08, it corrects a number of misidentifications at low column densities and augments the number of detections in light of new data and work by other research groups. Our catalog has 96 more H I absorbers and 28 more O VI absorbers than DS08. The increase can be attributed to the inclusion of new absorbers and sight lines as well as the more liberal splitting of absorbers into separate features. The corrected misidentifications were primarily weak metal lines mistaken for other species (e.g., Si III mistaken for Ly α) or uncommonly seen metals associated with high column density H I absorbers mistaken for H I. As a result, this catalog supercedes that of DS08 for most purposes.

3.1.2. Contamination in reported absorbers in STIS data

Our catalog contains 381 H I detections in the 20 sightlines for which both COS and STIS and/or FUSE data are present. Of these detections, only 330 are detected by COS as well as STIS, as depicted in Figure 2. In most

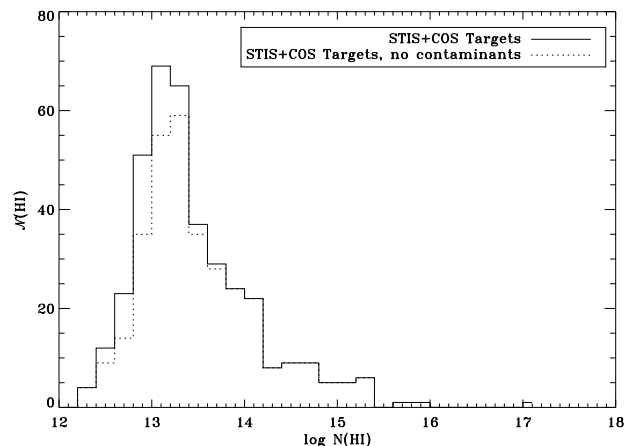


FIG. 2.— Histogram comparing detected H I absorbers for sight lines with both STIS and COS data. The solid line represents all detections, while the dotted line represents detections seen in both data sets.

cases, because the COS data have much higher S/N than the STIS data, this discrepancy suggests that some absorbers previously reported in the literature are in fact noise features rather than IGM absorption lines. For column densities $N_{\text{HI}} \lesssim 10^{13.2} \text{ cm}^{-2}$, between 20% and 40% of STIS detections are not supported by the COS data. In the column density range $10^{13.2} - 10^{13.6} \text{ cm}^{-2}$, this improves to around 5% to 10% contamination, while higher column densities are nearly entirely free from contami-

nation. These results suggest that censuses of the low-redshift Ly α forest at column densities below $10^{13.5} \text{ cm}^{-2}$ may suffer significant contamination in the form of line misidentification that is not accounted for in standard completeness corrections. Such contamination underscores the need for high-S/N observations of the IGM sensitive to Ly α equivalent widths $W_\lambda \approx 5 \text{ m}\text{\AA}$, corresponding to $\log N_{\text{HI}} \approx 12.0$.

3.2. Properties of the Absorbers

Table 6 summarizes our detection statistics for several ion species, listed in Column (1). The ions in the bottom half of the table have poor statistics, and should be viewed with skepticism. Columns (2) and (3) report the total number of 4σ detections in STIS data and the number of detections with false positives indicated by COS data removed, respectively. The latter number is the set of detections used in all statistics and derived quantities. Column (4) lists the range of redshifts that the survey covers for a given ion, while Column (5) lists the maximum redshift pathlength sampled at any sensitivity for the ion. Columns (6) through (8) report the absorber frequency per unit redshift pathlength integrated down to three equivalent widths. The survey is greater than 50% complete at the 30 m \AA scale, but at lower equivalent widths the completeness corrections take on a larger role. Finally, Column (9) provides a fit, in terms of the index β , to the distribution of absorbers as a function of column density per unit redshift,

$$\frac{d^2\mathcal{N}(> N)}{dz d\log N} \propto N^{-\beta}, \quad (14)$$

where we have used an error-weighted fit to the cumulative distributed histogram of $d\mathcal{N}/dz$. This distributed approach may systematically flatten the slope, β , by 0.05 – 0.1 dex relative to simple histograms (DS08).

In Table 8, we summarize our results for the baryon fraction for metal ions, $\Omega_{\text{IGM}}^{(\text{ion})}$ and Ω_{ion} , listed for equivalent widths integrated down to 10 m \AA and 30 m \AA . $\Omega_{\text{IGM}}^{(\text{ion})}$ is scaled by metallicity and peak ionization fraction as described above, and it is reported relative to the total baryon fraction, $\Omega_b = 0.0455 \pm 0.0028$ (Komatsu et al. 2011).

3.2.1. Individual Species

H I. — Our results for the column-density distribution of H I absorbers are presented in Figure 3. The histogram and $d\mathcal{N}/dz$ plots both exhibit a dip around $\log N_{\text{HI}} \approx 13.5$, which was also seen in DS08. The most likely explanation for this feature is that it is an artifact of the measurements arising from the detectability of higher-order Lyman lines. There is therefore more frequent use of COG measurements at column densities beyond this point. As discussed in Danforth et al. (2006), measurements of absorbers that exhibit only Ly α may be biased toward lower column densities. This effect may cause some absorbers to scatter into lower bins, creating the dip in the distribution near the transition between Ly α -only measurements and COG measurements. We expect that this effect has little impact on our absorber statistics, since it does not affect the total number of detections. A second dip is seen in the $d\mathcal{N}/dz$ plot at

$\log N_{\text{HI}} \approx 12.8$. It is not significant at the 95% confidence level, and the incompleteness correction dominates in this regime.

The entire distribution yields a power-law index, $\beta = 1.68 \pm 0.03$, in agreement with Penton et al. (2004), who found $\beta = 1.65 \pm 0.07$; Lehner et al. (2007), who found $\beta = 1.76 \pm 0.06$; and DS08, who found $\beta = 1.73 \pm 0.04$. Limiting the fit to bins that are greater than 50% complete, however, yields a slightly steeper value, $\beta = 1.74 \pm 0.04$, which may indicate systematic effects from our completeness corrections. The completeness-corrected line frequency integrated down to 30 m \AA ($\log N_{\text{HI}} \approx 12.74$) is $d\mathcal{N}/dz = 144_{-6}^{+7}$, in good agreement with Penton et al. (2004). DS08 found a lower value of $d\mathcal{N}/dz = 129_{-5}^{+6}$, where the discrepancy likely arises from the methodological differences described in Section 3.1.1.

The distribution of the Doppler parameter, b , for H I provides constraints on the thermal state of the IGM. The distribution of measured b -values, limited to absorbers with errors in b and N_{HI} less than 50%, is shown in Figure 4, with a range from $b = 6 - 137 \text{ km s}^{-1}$ with a mean, median, and standard deviation of 34, 30, and 17 km s^{-1} , respectively. Values of $b = (30 \text{ km s}^{-1})b_{30}$ correspond to a thermal temperature of $T \approx (54, 500 \text{ K})b_{30}^2$, but this number can be taken only as an upper limit because turbulence, bulk flows, and undetected subcomponents will inflate the measurements. The broad Ly α absorbers (BLAs) predicted by simulations and often associated with the WHIM (e.g., Richter et al. 2006) are difficult to characterize in the noisy STIS echelle data. Roughly 25% of our H I catalog has a measured $b > 40 \text{ km s}^{-1}$, but the errors are large in this regime. In addition to the large statistical errors, systematic effects such as unresolved subcomponents, insufficiently characterized AGN continua, and instrumental artifacts likely add further uncertainty to the upper end of the distribution of b -values. The treatment of BLAs is dealt with more carefully in Lehner et al. (2007) and Danforth et al. (2010), with the latter utilizing much higher S/N data from COS to further constrain their properties; we refer the interested readers to those works.

O VI. — We find a power-law index for the entire O VI distribution (Figure 5, top panels) of $\beta = 2.08 \pm 0.12$, in good agreement with our group’s previous work (Danforth & Shull 2008, 2005). Interestingly, we see a turnover in the $d\mathcal{N}/dz$ column density distribution at $\log N_{\text{OVI}} \approx 13.5$. This effect was also seen by Danforth & Shull (2005), albeit with just five absorbers at such low column densities. On the other hand, DS08 found no evidence of a turnover, with 26 absorbers in the bins at $\log N_{\text{OVI}} < 13.5$. We report 29 absorbers in our three lowest bins ($12.9 < \log N_{\text{OVI}} < 13.5$) over a larger pathlength in z . The turnover seems to arise from the combined effect of a stronger peak in the distribution of absorbers at $\log N_{\text{OVI}} \approx 13.6$ coupled with an increase of only 3 absorbers with $\log N_{\text{OVI}} < 13.5$ compared to DS08. Our correction of several absorbers from the DS08 catalog that were misidentified as O VI explains the lack of a large increase in the number of absorbers in these bins despite our larger pathlength. Despite its statistical

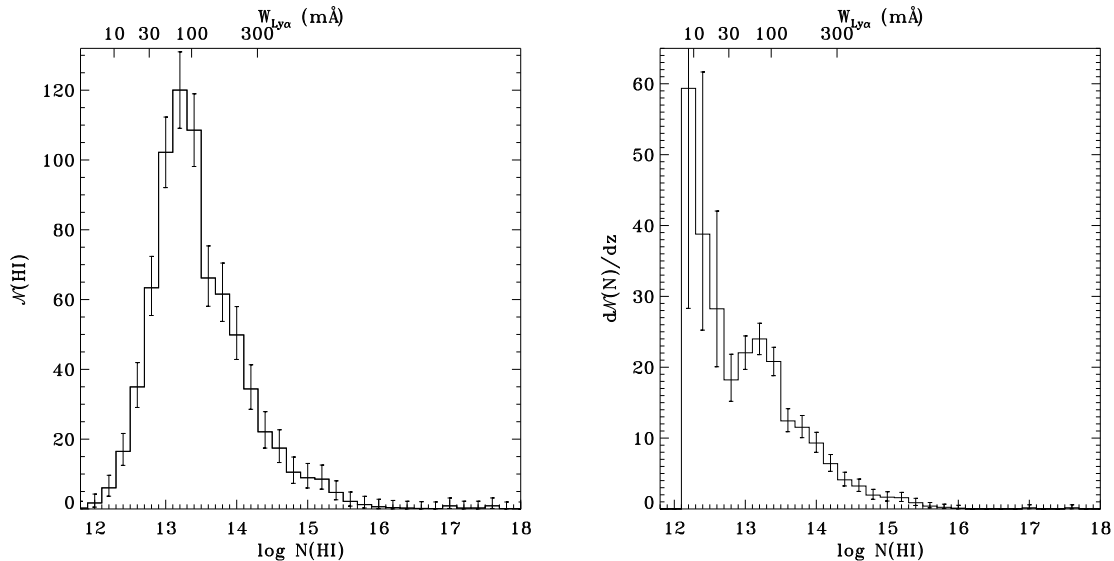


FIG. 3.— Distributed histograms of H I detection statistics and $\mathcal{N}(\text{HI}) \equiv d\mathcal{N}/dz$. Left panel shows the number of absorbers per 0.2 dex bin, uncorrected for completeness. Right panel shows the completeness-corrected differential $d\mathcal{N}/dz$ vs. $\log N_{\text{HI}}$. Error bars in both panels include one-sided Poisson errors, while the right panel errors also include contributions from Δz uncertainty.

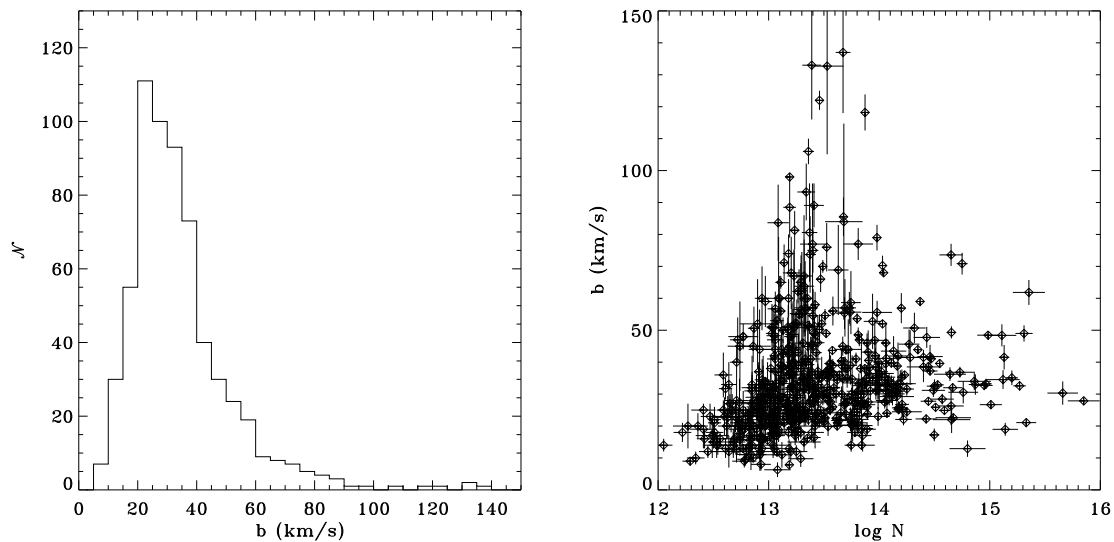


FIG. 4.— Distribution of Doppler b -parameters of 626 of 746 H I absorbers, limited to absorbers with errors in b and N_{HI} less than 50%. The median and sample standard deviation of the distribution are 30 km s^{-1} and 17 km s^{-1} , respectively. Because some absorbers may actually be multiple blended components, this distribution provides upper limits on b -values.

significance, the turnover should be treated with caution. The statistical errors on individual measurements at these column densities are quite large, and the method of catalog construction may introduce systematic biases at low column densities owing to the predominant reliance on the catalog of DS08 in that regime. It is also worth noting that our completeness corrections exceed 50% in these bins. A new COS survey at higher S/N will be required to conclusively address the issue of this turnover. If the turnover is real, it may be more realistic to apply the power-law formalism only to data with $\log N_{\text{OVI}} > 13.5$; this approach yields a much steeper slope, $\beta = 2.50 \pm 0.26$.

Our results for the frequency of O VI absorbers compare favorably to simulations. Smith et al. (2011) inves-

tigated the distribution using the N-body hydrodynamic code Enzo in a $50h^{-1}$ Mpc comoving box with 1024^3 grid cells (run 50_1024_2 in that work). Cooling in CIE and with both collisional and photoionization (C+P) were investigated. We plot their results for the cumulative distribution of $d\mathcal{N}(> N_{\text{OVI}})/dz$ against our empirical distribution in Figure 6. Though CIE adequately explains the distribution at high column densities, it over-predicts the distribution at lower column densities, suggesting an increasing role of photoionization at these scales. These smaller clouds may reside in areas of the IGM that are characterized by overall lower baryonic densities, making them more sensitive to the effects of photoionization. Alternately, perhaps they reside in the circumgalactic medium, where higher UV radiation fields may increase

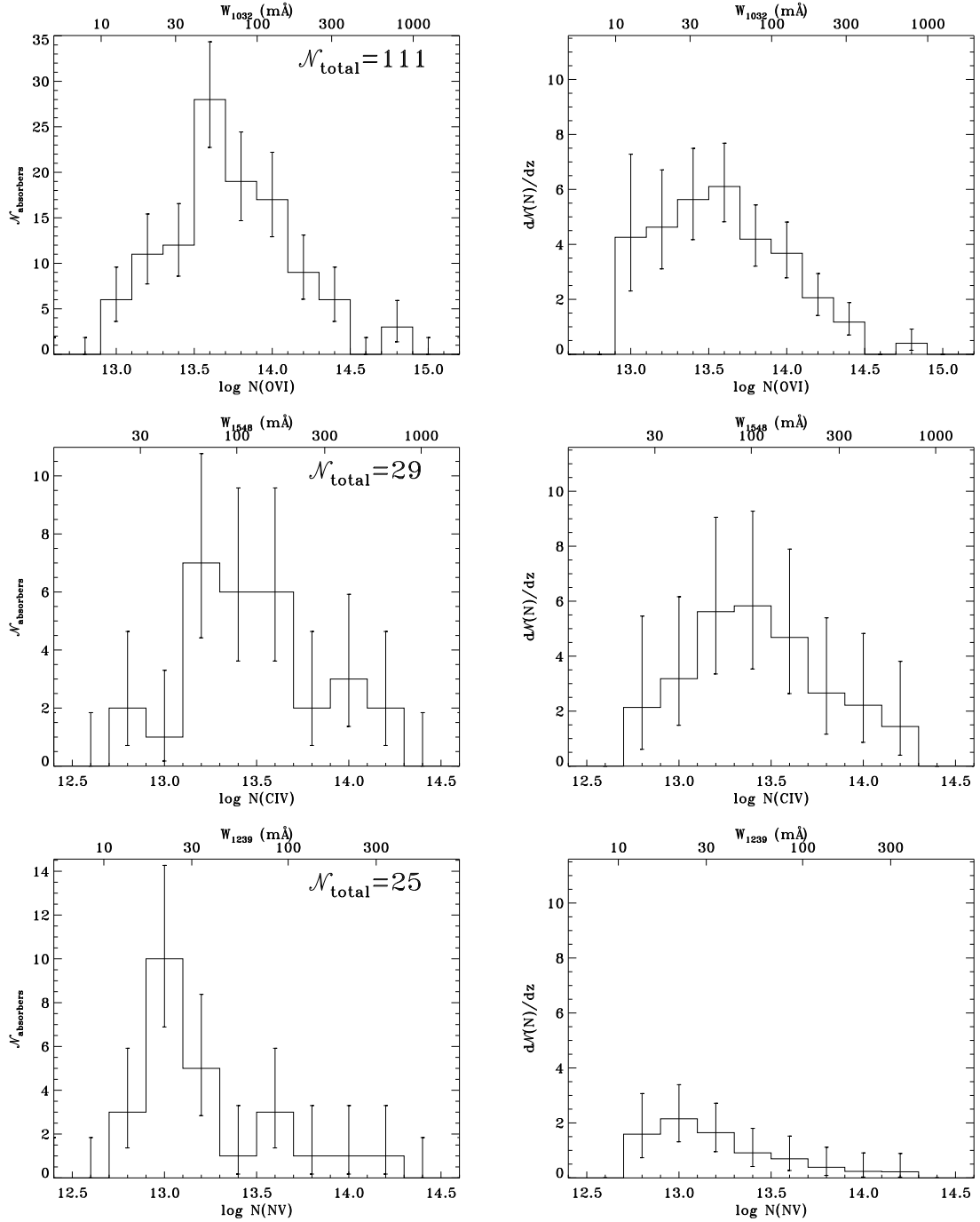


FIG. 5.— Simple histograms of detection statistics and distributed histograms of dN/dz vs. $\log N$ for O VI (top), C IV (middle), and N V (bottom).

the role of photoionization.

In Figure 7, we present the O VI Doppler b -parameter distribution, again limited to absorbers with errors in b and N_{OVI} less than 50%. Nearly all measurements in this distribution were performed using the the Voigt profile routine described previously, which accounts for instrumental resolution. The distribution spans a range of $b = 6 - 78 \text{ km s}^{-1}$ with a mean, median, and standard deviation of 32, 28, and 16 km s^{-1} , respectively, in excellent agreement with DS08. Qualitatively, the distribution is similar to Figure 13 of Tripp et al. (2008),

although they find a higher density of absorbers with $b < 10 \text{ km s}^{-1}$. We suspect that this discrepancy arises from their more aggressive splitting of systems into sub-components, which may artificially lower their distribution of b -values. Eleven absorbers (14%) in our catalog have b -values corresponding to temperatures at or below $10^{5.45} \text{ K}$, the peak in CIE. Only two (3%) correspond to temperatures less than 10^5 K as expected from photoionization.

To investigate the correlation of O VI absorption with H I absorption, we combined all components of each ion

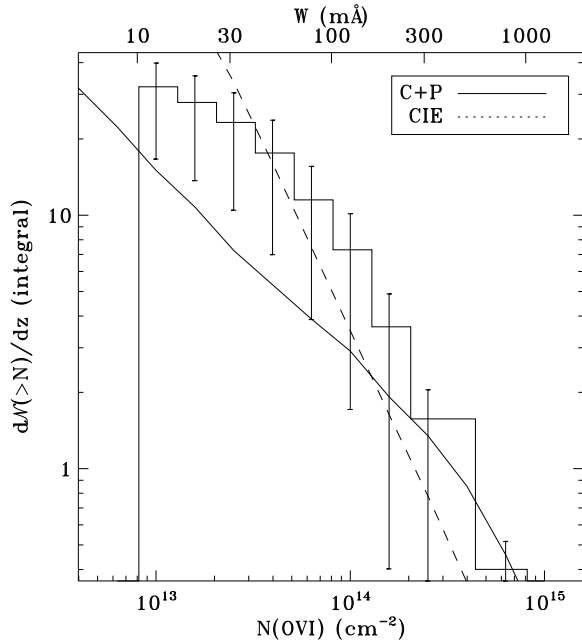


FIG. 6.— Cumulative $dN(>N)/dz$ for O VI absorbers compared to simulation results of run 50_1024_2 from Smith et al. (2011) featuring collisional and photoionization (C+P - solid line) and CIE cooling (dashed line).

species with $|\Delta v| \leq 50 \text{ km s}^{-1}$, yielding “systemic” column densities and velocity displacements. We then correlated the two set of absorbers, counting any O VI absorption with a redshift within several Δv offsets of the redshift of the H I as being associated with that H I absorber. The resulting distributions are plotted as histograms as a function of column density in Figure 8. The strongest H I absorption systems nearly always have associated O VI. In all but a handful of cases, O VI has associated H I absorption. We found four cases of O VI absorption without apparent associated H I absorption within $|\Delta v| \leq 100 \text{ km s}^{-1}$ and only one case without H I absorption within $|\Delta v| \leq 300 \text{ km s}^{-1}$. This kinematic association confirms that H I and O VI often arise in spatially associated, multiphase systems, as predicted by simulations (Cen & Ostriker 1999; Davé et al. 2001; Smith et al. 2011) and observed (Danforth & Shull 2008; Tripp et al. 2008; Savage et al. 2011b).

C IV and N V.— The Li-like C IV and N V ions have also been suggested as possible tracers of WHIM gas, although photoionization probably also plays a role for these species. We report 29 C IV absorbers, shown in Figure 5 (middle row), but our survey is sensitive to C IV over a much shorter total redshift pathlength ($\Delta z = 2.52$) compared to other ions. The distribution yields a power-law index of $\beta = 1.77 \pm 0.16$ and an absorber frequency integrated down to 30 mÅ ($\lambda 1548.2$; $\log N_{\text{CIV}} \approx 12.87$) of $dN/dz = 12_{-2}^{+4}$. Our C IV catalog has changed little since DS08, so, unsurprisingly, these results are in good agreement with the results from that study and its discussion of the ion. As in the O VI distribution, we see a turnover in the dN/dz column density distribution of C IV at $\log N_{\text{CIV}} \approx 13.2$, but it is not significant at the 95% confidence level. We invoke all of the same caveats in ascribing meaning to this feature as

we did for the O VI results.

Despite having more than double the redshift pathlength of C IV, the N V ion has only 25 absorbers, shown in Figure 5 (bottom row), yielding a power-law index of $\beta = 2.00 \pm 0.24$ and an absorber frequency integrated down to 30 mÅ ($\lambda 1238.2$; $\log N_{\text{NV}} \approx 13.15$) of $dN/dz = 10_{-3}^{+5}$. The low frequency of detections likely is attributable to the low abundance of nitrogen compared to oxygen or carbon. As a result, most detections are weak, and it will remain difficult to draw many conclusions from N V absorption until a systematic survey in more sensitive COS data is undertaken. The slight turnover apparent in the dN/dz column density distribution is not statistically significant.

C III, Si III, Si IV, Fe III and other ions.— C III and Si III are expected to arise in photoionized conditions, and they are well characterized by the high-resolution STIS data, owing to their relatively narrow line widths and strong absorption features. Our catalog’s primary differences from that of DS08 arise from a more careful treatment of the narrow subcomponents seen in many of these absorbers. We report 50 C III absorbers, shown in Figure 9 (top row), yielding a power-law index of $\beta = 1.86 \pm 0.09$ and an absorber frequency integrated down to 30 mÅ ($\log N_{\text{CIII}} \approx 12.67$) of $dN/dz = 14.4_{-2.2}^{+4.7}$. We find 57 Si III absorbers, shown in Figure 9 (second row), yielding a power-law index of $\beta = 1.74 \pm 0.10$ and an absorber frequency integrated down to 30 mÅ ($\log N_{\text{SiIII}} \approx 12.14$) of $dN/dz = 7.4_{-1.2}^{+2.1}$. We see no significant turnover in their dN/dz column density distributions.

We report 30 Si IV detections, shown in Figure 9 (third row), which follow a distribution quite similar to that found in DS08. They found a power-law index of $\beta = 1.92 \pm 0.17$ that was somewhat steeper than that of the other low-ionization state species. Our catalog yields an index of $\beta = 1.73 \pm 0.13$, bringing it more in line with the other ions. We find an absorber frequency integrated down to 30 mÅ ($\lambda 1393.8$; $\log N_{\text{SiIV}} \approx 12.53$) of $dN/dz = 9.2_{-2.8}^{+4.5}$.

DS08 made an ambitious attempt to characterize Fe III absorption in the IGM, reporting 14 detections comprising a steep distribution with $\beta = 2.2 \pm 0.4$. However, they expressed some caution about the validity of these results, owing to the high Fe III abundance ratios. Our reanalysis of the data suggests that all Fe III results should be treated with skepticism. Although we report 11 detections at the nominal 4σ level, nearly all detections for which COS data were available were revealed as misinterpreted noise features. It is thus likely that a significant number of those 11 absorbers may vanish, too, if observed at a higher S/N with COS. In reporting our Fe III statistics for this species in Table 6, we tentatively note that they are poorly constrained. Table 6 further reports our detections of several other low-ionization species. As with Fe III, we mark them as poorly constrained owing to the paucity of detections. No statistics are presented for N II ($\lambda 1084.0, \lambda 915.6$) or N III ($\lambda 989.8$) because no systematic search was made for these species. The listed detections were primarily serendipitous corrections of past misidentifications in the literature, and they are primarily associated with high column density H I absorption systems.

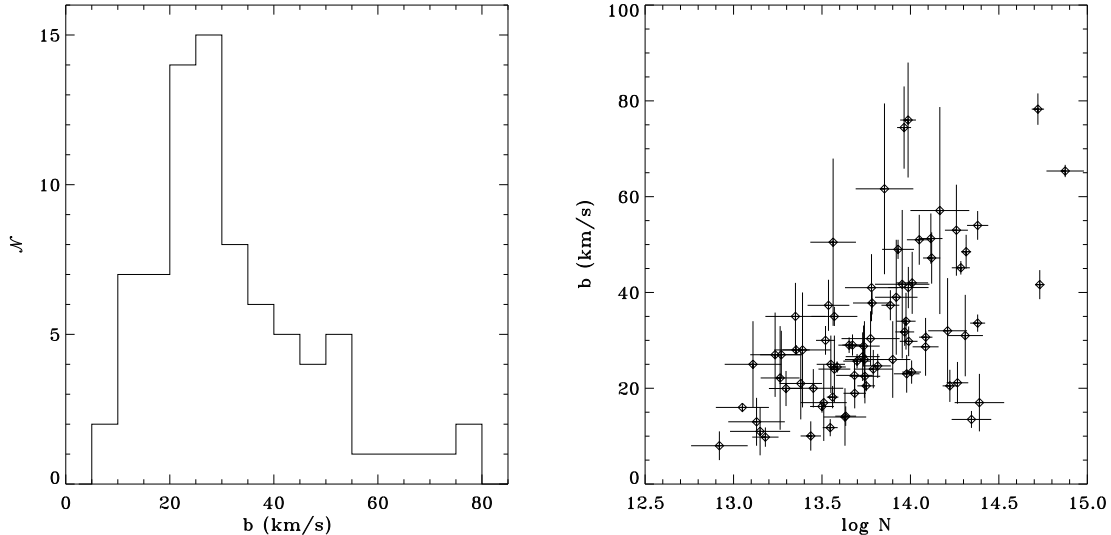


FIG. 7.— Distribution of Doppler b -parameters of 79 of 111 O VI absorbers, limited to absorbers with errors in b and N less than 50%. The median and sample standard deviation of the distribution are 28 km s^{-1} and 16 km s^{-1} , respectively. Because some absorbers may actually be multiple blended components, this distribution provides upper limits on b -values.

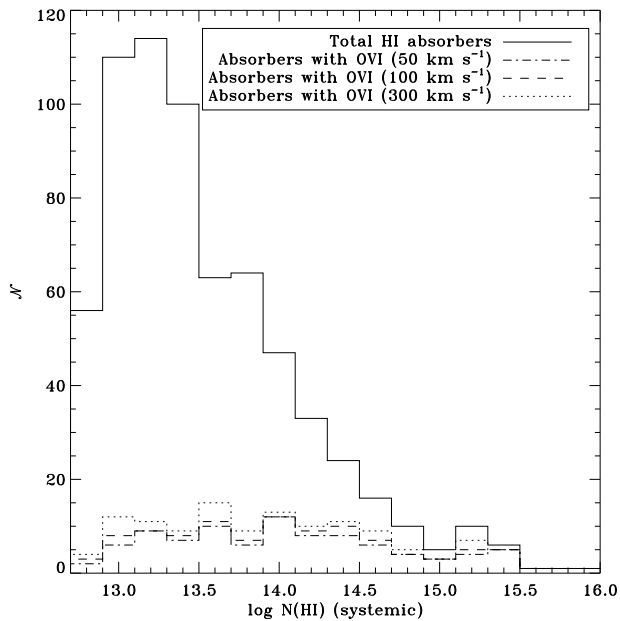


FIG. 8.— Histograms of all “systemic” H I absorbers (see Section 3.2.1.0 for details), in which subcomponents within 50 km s^{-1} of each other have been combined (solid line), and systems with O VI absorbers within 50 km s^{-1} (dotted line), 100 km s^{-1} (dashed line), and 200 km s^{-1} (dash dotted line) of the systemic H I redshift.

3.3. The Baryon Density of the IGM

Using the assumptions for metallicity and ionization fraction described above, the three best tracers of the WHIM yield estimates of the fractional baryon content that they trace as $\Omega_{\text{IGM}}^{(\text{ion})}/\Omega_b \approx 9 \pm 1\%$ (O VI), $6 \pm 3\%$ (N V), and $7 \pm 1\%$ (C IV). DS08 offered several interpretations for variations in these values. Most obviously, the differences may arise due to dominant systematic errors arising from our assumed CIE ion fractions or metallicities, or they may arise simply due to line sensitivity

variations in the data itself. That work also suggested that perhaps their values (9%, 5%, and 3% for O VI, N V, and C IV, respectively) represented a true gradient the WHIM baryon density as a function of temperature, because their derived densities follow the trend in peak CIE temperatures. This interpretation is not supported by our improved values, though we are unable to rule it out.

The largest systematic uncertainties in these values arise from the metallicity and ionization fraction assumptions. In the above values, we assume a metallicity of 10% solar and an ionization fraction corresponding to peak CIE value. Recent simulations (Shull et al. 2011) suggest that the weighted mean product of these quantities may be closer to $f_{\text{OVI}}(Z/Z_{\odot}) = 0.01$, half of our assumed value of 0.02. Using this number in our calculations effectively doubles the baryonic content traced by O VI, yielding $\Omega_{\text{IGM}}^{(\text{ion})}/\Omega_b \approx 17.2 \pm 1.4\%$. Shull et al. (2011) also report a column density dependent fit to this quantity: $f_{\text{OVI}}(Z/Z_{\odot}) = (0.015)[N_{\text{OVI}}/10^{14} \text{ cm}^{-2}]^{0.70}$. Evaluating that fit separately for each bin in our Ω calculations raises the baryonic content still further, to $\Omega_{\text{IGM}}^{(\text{ion})}/\Omega_b \approx 18.9 \pm 2.0\%$, but the scatter in the $f_{\text{OVI}}Z$ fit is roughly 0.35 dex. Simulations suggest, however, that the actual contribution of O VI to Ω_b , as calculated by the direct summation of O VI within the simulation, may be as much as 10 – 40% higher than that derived from absorption-line studies, as traced by the creation of synthetic spectra from the simulation (Smith et al. 2011). We can apply the analogous results from the same simulation, derived from run 50-1024-2 from Smith et al. (2011) (B.D. Smith, private communication), to our N V and C IV results. Using the column density fits for these ions, we obtain baryon fractions of $10.1 \pm 6.0\%$ (N V) and $22.3 \pm 3.7\%$ (C IV). The C IV results change most dramatically, possibly because it is likely to be more sensitive to photoionization effects.

The baryon content of the photoionized Ly α forest has been well studied elsewhere. Penton et al. (2004) ac-

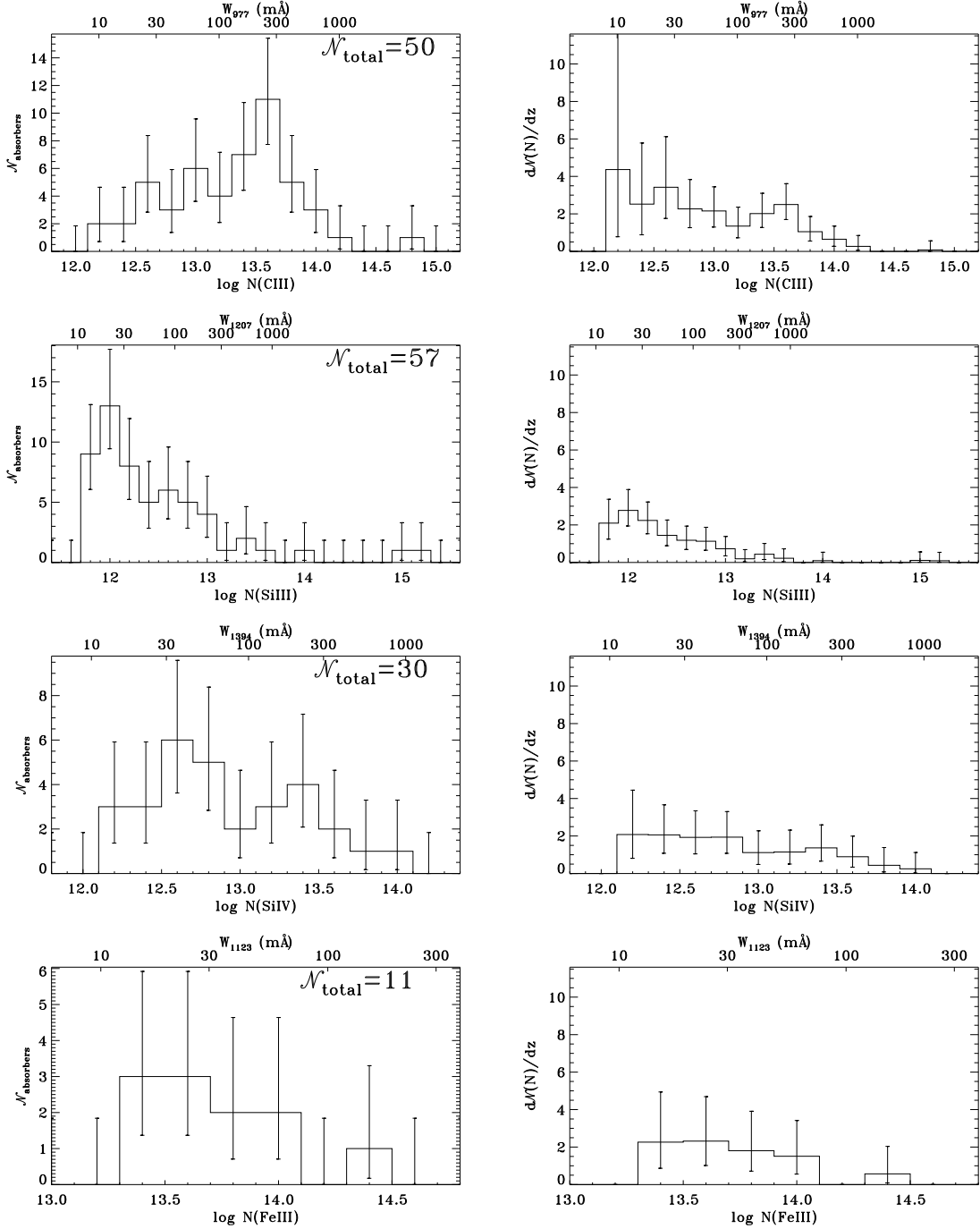


FIG. 9.— Simple histograms of detection statistics and distributed histograms of $d\mathcal{N}/dz$ vs. $\log N$ for C III (top), Si III (second row), Si IV (third row), and N V (bottom).

counted for roughly 29% of the local baryon mass down to $\log N_{\text{HI}} = 12.5$, and Lehner et al. (2007) found a similar estimate of around 30%. We present our own calculations based on the methods described in Section 2.4.2 in Table 7. The Shull et al. (2011) method is most appropriate at lower column densities, while the Schaye (2001) method, which assumes gravitationally bound clouds, is likely more appropriate at higher column densities. In estimating a total ratio $\Omega_{\text{Ly}\alpha}/\Omega_b$, a cutoff between the two methods should be assumed. Taking a cutoff of $\log N_{\text{HI}} = 14.5$, corresponding to the transition

in the slope of the column density distribution seen by Penton et al. (2004), we find $\Omega_{\text{Ly}\alpha}/\Omega_b = 20.9 \pm 2.0\%$. If the cutoff is instead drawn at $\log N_{\text{HI}} = 16.5$, we find $\Omega_{\text{Ly}\alpha}/\Omega_b = 23.7 \pm 2.2\%$. Because this calculation is model dependent, systematic errors likely dominate over the statistical errors that we report.

The baryon fractions reported in Table 8 for the lower-ionization species likely trace a metal-enriched subset of the gas in the Ly α forest. As a result, they are probably photoionized, rendering assumptions regarding the ionization fraction problematic. Hence, the values

TABLE 7
BARYON CONTENT OF THE LOCAL $\text{Ly}\alpha$ FOREST

$\log N_{\text{HI}}$ Range	\mathcal{N}	$\Omega_{\text{Ly}\alpha}$ ^a	$\Omega_{\text{Ly}\alpha}/\Omega_b$ (%) ^a	$\Omega_{\text{Ly}\alpha}$ ^b	$\Omega_{\text{Ly}\alpha}/\Omega_b$ (%) ^b	$\Omega_{\text{Ly}\alpha}$ ^c	$\Omega_{\text{Ly}\alpha}/\Omega_b$ (%) ^c
12.0 – 12.5	20	0.0055 ± 0.0043	12.0 ± 9.5	0.0038 ± 0.0041	8.3 ± 9.0	0.0036 ± 0.0041	8.0 ± 8.9
12.5 – 13.5	427	0.0044 ± 0.0010	9.8 ± 2.2	0.0039 ± 0.0008	8.6 ± 1.8	0.0038 ± 0.0008	8.4 ± 1.7
13.5 – 14.5	244	0.0031 ± 0.0003	6.7 ± 0.6	0.0038 ± 0.0003	8.4 ± 0.8	0.0038 ± 0.0003	8.3 ± 0.7
14.5 – 15.5	49	0.0012 ± 0.0002	2.7 ± 0.5	0.0023 ± 0.0004	5.0 ± 1.0	0.0022 ± 0.0004	4.9 ± 0.9
15.5 – 16.5	3	0.0001 ± 0.0001	0.3 ± 0.2	0.0003 ± 0.0002	0.7 ± 0.4	0.0003 ± 0.0002	0.7 ± 0.4
12.5 – 14.5	671	0.0075 ± 0.0010	16.5 ± 2.3	0.0077 ± 0.0009	17.0 ± 1.9	0.0076 ± 0.0008	16.6 ± 1.8
14.5 – 16.5	52	0.0013 ± 0.0002	2.9 ± 0.5	0.0026 ± 0.0005	5.7 ± 1.0	0.0026 ± 0.0005	5.7 ± 1.0
16.5 – 19.0	3	0.0006 ± 0.0004	1.4 ± 0.8	0.0035 ± 0.0022	7.8 ± 4.8	0.0035 ± 0.0021	7.7 ± 4.7
12.5 – 16.5	723	0.0088 ± 0.0011	19.4 ± 2.3	0.0103 ± 0.0010	22.7 ± 2.2	0.0102 ± 0.0010	22.3 ± 2.1
12.5 – 19.0	726	Shull method for $\log N_{\text{HI}} < 16.5$, Schaye method for $\log N_{\text{HI}} > 16.5$:				0.0108 ± 0.0010	23.7 ± 2.2

^a Method of Penton et al. (2000)

^b Method of Schaye (2001)

^c Method of Shull et al. (2011)

TABLE 8
SUMMARY OF IGM BARYON FRACTION RESULTS

Ion	$\Omega_{\text{ion}} (10^{-8})$		$\Omega_{\text{IGM}}^{(\text{ion})}/\Omega_b$ ^a	
	(> 10 mÅ)	(> 30 mÅ)	(> 10 mÅ)	(> 30 mÅ)
O VI	48.22 ± 3.77	40.33 ± 4.28	0.086 ± 0.007	0.072 ± 0.008
N V	4.19 ± 2.25	2.42 ± 2.85	0.059 ± 0.032	0.034 ± 0.040
C IV	20.11 ± 2.01	19.83 ± 2.06	0.067 ± 0.007	0.066 ± 0.007
C III	10.83 ± 1.38	8.75 ± 1.46	0.013 ± 0.002	0.010 ± 0.002
Si IV	11.07 ± 1.57	10.78 ± 1.78	0.099 ± 0.014	0.097 ± 0.016
Si III	17.53 ± 3.21	17.26 ± 4.27	0.061 ± 0.011	0.060 ± 0.015
Fe III	40.16 ± 14.31	29.48 ± 16.93	0.082 ± 0.029	0.060 ± 0.035

^a Scaled by f_{ion} , Z , and H_0 ; $\Omega_b = 0.0455 \pm 0.0028$ (Komatsu et al. 2011). See text for details.

of $\Omega_{\text{IGM}}^{(\text{ion})}/\Omega_b$ for these ions are extremely uncertain beyond the statistical errors given in the table. Recalculating them with column density dependent fits from the Smith et al. (2011) simulation gives values 2 to 3 times higher, but this huge variation likely indicates imperfections in the combined ionization calculations in simulations to date.

4. CONCLUSIONS AND SUMMARY

We have presented a comprehensive, critically evaluated catalog of low-redshift IGM absorbers present in archival legacy STIS and FUSE data. New data from COS informed the evaluation, revealing past errors in the interpretation of absorption lines. We analyzed 44 sightlines, yielding 746 H I absorbers over a total $\text{Ly}\alpha$ redshift pathlength of $\Delta z = 5.38$. In addition, we reported on 111 O VI absorbers, 29 C IV absorbers, and made numerous detections of other ion species (N V, C III, Si III, Si IV).

Our O VI results found distributions comparable to those found in past work. We found a $d\mathcal{N}/dz$ turnover at low column densities similar to that seen by Danforth & Shull (2005) but absent in DS08. Using a more sophisticated baryon accounting technique than previous work, we estimated from our empirical distribution of absorbers that the WHIM contributes roughly 19% of the total baryonic density, Ω_b . We discussed several significant systematic uncertainties in deriving such a quantity, most notably corrections for the metallicity

and ionization state of the IGM. We presented similar distributions and quantities derived from N V and C IV detections, of which we reported 25 and 29 absorbers, respectively. Similar statistics were reported for other ion species at lower ionization states, and we summarized these results in Table 6. In particular, we found that past studies of Fe III absorption in the low-redshift IGM suffer from significant contamination due to line misidentification.

Our catalog of 746 H I absorbers follows a similar distribution to that of our group's past work in this field. DS08 used an incorrect cosmological factor to derive baryon densities from the detections; we corrected that error with our new catalog, accounting for roughly 24% of Ω_b with $\text{Ly}\alpha$ forest detections. Taken together with inferred WHIM baryon densities, our catalog accounts for $\sim 43\%$ of Ω_b in the low-redshift IGM. Unfortunately, the present catalog is unable to adequately probe broad $\text{Ly}\alpha$ absorbers, which are expected to trace significant baryonic content in the WHIM. Such absorbers require high S/N data, better supplied by future work with COS.

This paper has analyzed most of the IGM absorption-line systems at $z < 0.4$ observed by STIS. With COS, one can take these studies much further through a spectroscopic survey of the structure, metallicity, and physical conditions of the IGM and CGM. Observing the relation of IGM absorption systems to galaxy distributions will be

achieved through uniformly processed, high-S/N spectra and an unbiased sample of IGM and CGM absorbers, including the Ly α forest, metal-line systems, Lyman-limit systems, and partial-limit systems. We have proposed a sensitive (S/N \sim 30) HST Spectroscopic Legacy Survey of the low-redshift IGM and CGM toward AGN selected for UV brightness and total redshift pathlength. These absorbers will be compared with deep galaxy surveys, thereby connecting galaxies to large-scale structure and inferring the extent of feedback. These projects will produce a complete legacy survey of gas and ($L > L_{\text{SMC}}$) galaxies, located within 1-2 Mpc of the ($z = 0.1 - 0.4$) absorbers. The high UV sensitivity of COS provides an excellent tool for studying gas in multiple thermal phases and metallicities in the low-redshift IGM and CGM. These studies are best done at low redshift ($z \leq 0.4$), allowing us to use correlations of the absorbers with distributions of galaxies, particularly those of low mass and luminosity ($L < L^*$) which contribute significant radiative, thermal, and chemical feedback. While the catalog presented here represents an improvement to our census of IGM baryonic content, these future studies with COS

will be able to address conclusively the distributions of absorbers at low column densities and broad line widths. Poorly constrained ions such as Fe III and N V may be probed with more reliability, and the increase in pathlength will dramatically improve the statistics of all ion species addressed here.

The authors would like to thank Thorsten Tepper-García for helpful comments regarding the errors in DS08 and Britton Smith for his contributions regarding simulation results for the metallicity and ionization state of the IGM. This work was supported by Space Telescope Science Institute Archive Legacy grant AR-11773.01, NSF grant AST07-07474, and STScI COS-support grant NNX08-AC14G. This work made use of observations made with the NASA/ESA *Hubble Space Telescope*, obtained from the data archive at the STScI. STScI is operated by the Association of Universities for Research in Astronomy, Inc., under NASA contract NAS5-26555.

Facilities: FUSE, HST (COS, STIS).

REFERENCES

- Aracil, B., Tripp, T. M., Bowen, D. V., Prochaska, J. X., Chen, H.-W., & Frye, B. L. 2006, MNRAS, 367, 139
- Asplund, M., Grevesse, N., Sauval, A. J., & Scott, P. 2009, ARA&A, 47, 481
- Bahcall, J. N., & Peebles, P. J. E. 1969, ApJ, 156, L7
- Cen, R., & Fang, T. 2006, ApJ, 650, 573
- Cen, R., & Ostriker, J. P. 1999, ApJ, 519, L109
- Danforth, C. W., Keeney, B. A., Stocke, J. T., Shull, J. M., & Yao, Y. 2010, ApJ, 720, 976
- Danforth, C. W., & Shull, J. M. 2005, ApJ, 624, 555
- . 2008, ApJ, 679, 194
- Danforth, C. W., Shull, J. M., Rosenberg, J. L., & Stocke, J. T. 2006, ApJ, 640, 716
- Danforth, C. W., Stocke, J. T., Keeney, B. A., Penton, S. V., Shull, J. M., Yao, Y., & Green, J. C. 2011, ApJ, 743, 18
- Davé, R., et al. 2001, ApJ, 552, 473
- Ganguly, R., Masiero, J., Charlton, J. C., & Sembach, K. R. 2003, ApJ, 598, 922
- Gehrels, N. 1986, ApJ, 303, 336
- Green, J. C., et al. 2012, ApJ, 744, 60
- Haardt, F., & Madau, P. 2012, ApJ, 746, 125
- Howk, J. C., Ribaldo, J. S., Lehner, N., Prochaska, J. X., & Chen, H.-W. 2009, MNRAS, 396, 1875
- Jenkins, E. B., Bowen, D. V., Tripp, T. M., Sembach, K. R., Leighly, K. M., Halpern, J. P., & Lauroesch, J. T. 2003, AJ, 125, 2824
- Komatsu, E., et al. 2011, ApJS, 192, 18
- Lehner, N., Savage, B. D., Richter, P., Sembach, K. R., Tripp, T. M., & Wakker, B. P. 2007, ApJ, 658, 680
- Lehner, N., Savage, B. D., Wakker, B. P., Sembach, K. R., & Tripp, T. M. 2006, ApJS, 164, 1
- Moos, H. W., et al. 2000, ApJ, 538, L1
- Morton, D. C. 2003, ApJS, 149, 205
- Narayanan, A., et al. 2011, ApJ, 730, 15
- Oegerle, W. R., et al. 2000, ApJ, 538, L23
- Peimbert, M., Luridiana, V., & Peimbert, A. 2007, ApJ, 666, 636
- Penton, S. V., Shull, J. M., & Stocke, J. T. 2000, ApJ, 544, 150
- Penton, S. V., Stocke, J. T., & Shull, J. M. 2004, ApJS, 152, 29
- Prochaska, J. X., Chen, H.-W., Howk, J. C., Weiner, B. J., & Mulchaey, J. 2004, ApJ, 617, 718
- Ralchenko, Y., Kramida, A., Reader, J., & NIST ASD Team. 2010, NIST Atomic Spectra Database (version 4.0)
- Richter, P., Fang, T., & Bryan, G. L. 2006, A&A, 451, 767
- Richter, P., Savage, B. D., Tripp, T. M., & Sembach, K. R. 2004, ApJS, 153, 165
- Richter, P., Savage, B. D., Wakker, B. P., Sembach, K. R., & Kalberla, P. M. W. 2001, ApJ, 549, 281
- Savage, B. D., Lehner, N., & Narayanan, A. 2011a, ApJ, 743, 180
- Savage, B. D., Narayanan, A., Lehner, N., & Wakker, B. P. 2011b, ApJ, 731, 14
- Savage, B. D., Sembach, K. R., Tripp, T. M., & Richter, P. 2002, ApJ, 564, 631
- Savage, B. D., Wakker, B. P., Fox, A. J., & Sembach, K. R. 2005, ApJ, 619, 863
- Schaye, J. 2001, ApJ, 559, 507
- Sembach, K. R., Howk, J. C., Savage, B. D., Shull, J. M., & Oegerle, W. R. 2001, ApJ, 561, 573
- Sembach, K. R., & Savage, B. D. 1992, ApJS, 83, 147
- Sembach, K. R., Tripp, T. M., Savage, B. D., & Richter, P. 2004, ApJS, 155, 351
- Shull, J. M., Roberts, D., Giroux, M. L., Penton, S. V., & Fardal, M. A. 1999, AJ, 118, 1450
- Shull, J. M., Smith, B. D., & Danforth, C. W. 2011, ArXiv e-prints
- Smith, B. D., Hallman, E. J., Shull, J. M., & O'Shea, B. W. 2011, ApJ, 731, 6
- Sutherland, R. S., & Dopita, M. A. 1993, ApJS, 88, 253
- Thom, C., & Chen, H.-W. 2008, ApJS, 179, 37
- Tripp, T. M., Giroux, M. L., Stocke, J. T., Tumlinson, J., & Oegerle, W. R. 2001, ApJ, 563, 724
- Tripp, T. M., Sembach, K. R., Bowen, D. V., Savage, B. D., Jenkins, E. B., Lehner, N., & Richter, P. 2008, ApJS, 177, 39
- Tumlinson, J., Shull, J. M., Giroux, M. L., & Stocke, J. T. 2005, ApJ, 620, 95
- Weymann, R. J., Vogel, S. N., Veilleux, S., & Epps, H. W. 2001, ApJ, 561, 559
- Williger, G. M., Heap, S. R., Weymann, R. J., Davé, R., Ellingson, E., Carswell, R. F., Tripp, T. M., & Jenkins, E. B. 2006, ApJ, 636, 631